

FAINT SUBMILLIMETER GALAXIES REVEALED BY MULTIFIELD DEEP ALMA OBSERVATIONS:  
NUMBER COUNTS, SPATIAL CLUSTERING, AND DARK SUBMILLIMETER EMITTERSYOSHIAKI ONO<sup>1</sup>, MASAMI OUCHI<sup>1,2</sup>, YASUTAKA KURONO<sup>3</sup>, AND RIEKO MOMOSE<sup>1</sup>*submitted to ApJ*

## ABSTRACT

We present the statistics of faint submillimeter/millimeter galaxies (SMGs) and serendipitous detections of submillimeter/millimeter emitters (SMEs) with no multi-wavelength continuum counterpart revealed by the deep ALMA observations. We identify faint SMGs with flux densities of 0.1 – 1.0 mJy in the deep Band 6 and Band 7 maps of 10 independent fields that reduce cosmic variance effects. The differential number counts at 1.2 mm are found to increase with decreasing flux density down to 0.1 mJy. Our number counts indicate that the faint (0.1 – 1.0 mJy, or  $\text{SFR}_{\text{IR}} \sim 30 - 300 M_{\odot} \text{ yr}^{-1}$ ) SMGs contribute nearly a half of the extragalactic background light (EBL), while the remaining half of the EBL is mostly contributed by very faint sources with flux densities of  $< 0.1$  mJy ( $\text{SFR}_{\text{IR}} \lesssim 30 M_{\odot} \text{ yr}^{-1}$ ). We conduct counts-in-cells analysis with the multifield ALMA data for the faint SMGs, and obtain a coarse estimate of galaxy bias,  $b_g \approx 2$ . The galaxy bias suggests that the dark halo masses of the faint SMGs are  $\sim 10^{12} M_{\odot}$ , about an order of magnitude smaller than those of bright ( $> 1$  mJy) SMGs, but comparable with abundant high- $z$  star-forming populations such as sBzKs, LBGs, and LAEs. Finally, we report the serendipitous detections of SMEs with continuum counterparts neither in our 1.2 mm-band nor multi-wavelength images including ultra deep *HST*/WFC3 and *Spitzer* data. One of the SMEs has a significant line at 249.9 GHz with a signal-to-noise ratio of 7.1. If the SME is not a spurious source made by unknown systematic noise of ALMA, the strong upper limits of our multi-wavelength data suggest that the SME is a faint galaxy at  $z \gtrsim 6$ .

*Subject headings:* galaxies: formation — galaxies: evolution — galaxies: high-redshift

## 1. INTRODUCTION

In the past decades, it has been found that the amount of the cosmic infrared (IR) background is comparable to that of the cosmic optical background (Puget et al. 1996; Fixsen et al. 1998; Hauser et al. 1998; Hauser & Dwek 2001; Dole et al. 2006). The large amount of energy in the IR indicates that a significant fraction of the star formation in the universe is hidden by dust. Probing far-infrared (FIR) sources is key to a full understanding of galaxy formation history, and can provide strong constraints on models of galaxy formation (e.g., Granato et al. 2004; Baugh et al. 2005; Fontanot et al. 2007; Shimizu et al. 2012; Hayward et al. 2013).

Considerable progress has been made in charting the abundance of FIR sources (see the recent review of Casey et al. 2014) and shown that the extragalactic background light (EBL) at submillimeter and millimeter wavelengths is largely contributed by dusty star-forming galaxies, the so-called submillimeter galaxies (SMGs; Lagache et al. 2005). With a 15-m dish, the James Clerk Maxwell Telescope (JCMT) blank-field 850  $\mu\text{m}$  submillimeter surveys with Submillimeter Common User Bolometer Array (SCUBA; Holland et al. 1999) have resolved  $\sim 20 - 30\%$  of the 850  $\mu\text{m}$  EBL into distinct, bright SMGs with  $S_{850\mu\text{m}} > 2$  mJy (e.g., Barger et al. 1998;

Hughes et al. 1998; Barger et al. 1999; Eales et al. 1999, 2000; Scott et al. 2002; Borys et al. 2003; Wang et al. 2004; Coppin et al. 2006). Similar results have been obtained at 870  $\mu\text{m}$  with the Large APEX Bolometer Camera (LABOCA; Siringo et al. 2009) on the 12-m APEX telescope (Weiß et al. 2009). At 1.1 mm, about 6 – 10 % of the EBL has been resolved into individual sources by deep surveys with the AzTEC camera (Wilson et al. 2008) on both the JCMT (e.g., Perera et al. 2008; Austermann et al. 2009, 2010) and the 10-m Atacama Submillimeter Telescope Experiment (ASTE; e.g., Aretxaga et al. 2011; Scott et al. 2010; Hatsukade et al. 2011; Scott et al. 2012).

The biggest challenge for constructing the number counts of SMGs from such observations is the coarse spatial resolutions of the single-dish telescopes. Poor resolutions impose a fundamental limitation, the confusion limit (Condon 1974), on our ability to directly detect faint SMGs due to confusion noises. For instance, blank-field SCUBA surveys cannot reach the sensitivities required to identify the faint population below 2 mJy at 850  $\mu\text{m}$ . However, since the fraction of the millimeter and submillimeter EBL above 2 mJy is not large, the total EBL is likely dominated by the population below the limit. Observations of massive galaxy cluster fields push the detection limits of intrinsic flux density toward fainter ones thanks to gravitational lensing effects (e.g., Smail et al. 1997, 2002; Cowie et al. 2002; Knudsen et al. 2008; Johansson et al. 2011; Chen et al. 2013), but the positional uncertainties of the SMGs cause large uncertainties in the amplifications and the intrinsic fluxes (Chen et al. 2011).

Another issue which arises from the poor resolutions

ono@icrr.u-tokyo.ac.jp

<sup>1</sup> Institute for Cosmic Ray Research, The University of Tokyo, Kashiwa, Chiba 277-8582, Japan<sup>2</sup> Kavli Institute for the Physics and Mathematics of the Universe (Kavli IPMU), WPI, The University of Tokyo, Kashiwa, Chiba 277-8583, Japan<sup>3</sup> Joint ALMA Observatory, Alonso de Cordova 3107, Vitacura, Santiago 763-0355, Chile

is source blending; it is possible that several faint SMGs within a beam appear as a single brighter SMG. Source blending possibly changes the shape of the number counts, most critically by mimicking a population of bright SMGs. Multiplicity in a single-dish beam is also expected from evidence of strong clustering among SMGs (e.g., Blain et al. 2004; Scott et al. 2006; Weiß et al. 2009; Hickox et al. 2012). In fact, interferometric observations have shown that close pairs are common among SMGs and a significant fraction of bright SMGs found by single-dish observations are resolved into multiple sources (e.g., Ivison et al. 2007; Wang et al. 2011; Smolčić et al. 2012; Barger et al. 2012). To construct more reliable number counts down to flux densities of  $< 1$  mJy, we need to conduct deep surveys with high angular resolution.

The Atacama Large Millimeter/submillimeter Array (ALMA) enables us to explore faint (0.1–1.0 mJy) SMGs without effect of confusion limit thanks to its high sensitivity and high angular resolution. Hatsukade et al. (2013) have shown the potential of ALMA; they have obtained number counts of unlensed faint SMGs down to sub-mJy level using ALMA. However, their maps are continuous and the total survey area is not large, which may induce uncertainties in their measurements.

The physical properties of faint SMGs and their relationships with other galaxy populations found at similar redshifts have not yet been investigated well. The IR luminosities of the faint SMGs with 1.2 mm flux densities of 0.1–1.0 mJy are estimated to be  $L_{\text{IR}} \sim (1.5 - 15) \times 10^{11} L_{\odot}$ , if we adopt a modified black-body with typical values for SMGs, i.e., spectral index of  $\beta_{\text{d}} = 1.5$  and dust temperature of  $T_{\text{d}} = 35$  K (e.g., Kovács et al. 2006; Coppin et al. 2008), located at  $z = 2.5$  (e.g., Chapman et al. 2005; Yun et al. 2012). In this case, from the estimated IR luminosities, their obscured star-formation rates (SFRs) are calculated to be  $\text{SFR}_{\text{IR}} \sim 30 - 300 M_{\odot} \text{ yr}^{-1}$  (Kennicutt 1998b). Recently, *Herschel* observations have revealed that typical UV-selected galaxies such as Lyman-break galaxies (LBGs) have a median IR luminosity of  $L_{\text{IR}} \simeq 2.2 \times 10^{11} L_{\odot}$  (Reddy et al. 2012, see also Lee et al. 2012; Davies et al. 2013), which is comparable to that of the faint SMGs. From a stacking analysis of *Herschel* and ALMA data, Decarli et al. (2014) have found that *K*-selected galaxies including star-forming BzK galaxies (sBzKs) have IR luminosities of  $L_{\text{IR}} = (5 - 11) \times 10^{11} L_{\odot}$ . These results suggest that some of the faint SMGs might be FIR counterparts of UV- and/or *K*-selected galaxies.

The spatial clustering of SMGs is an important observable, since its strength can be used to estimate an average mass of their hosting dark matter haloes. Blain et al. (2004) have measured the clustering length of SMGs brighter than 5 mJy at  $850 \mu\text{m}$ , and found that the clustering length is significantly larger than those of optical/UV color-selected galaxies at similar redshifts, suggesting that SMGs are hosted by very massive dark haloes, with dark halo masses of  $M_{\text{DH}} \sim 10^{13} M_{\odot}$  (see also, Webb et al. 2003; Weiß et al. 2009; Hickox et al. 2012). Although several studies have investigated the clustering properties of SMGs, little attempt has been made for measuring those of faint SMGs with sub-mJy flux densities. This is because the previous large area sur-

veys with the single-dish telescopes cannot detect faint SMGs due to the confusion limit.

In this paper, we make use of multifield deep ALMA data, i.e., our own data for two independent fields and archival data with relatively long integration times, taken with the ALMA Band 6 and Band 7. We focus on serendipitously detected sources other than the targeted sources. The combination of the results of the deep ALMA surveys and those of a wide area survey in the literature yields robust estimates on the number counts of SMGs over a wide range of flux densities ( $\simeq 0.1 - 5$  mJy), which will be one of the most reliable estimates on the abundance of SMGs. In addition, from the field-to-field scatter in their number counts, we carry out a pathfinder study for estimating the clustering properties of the faint SMGs.

Finally, we conduct a blind search for line emitters at 1.2 mm using the ALMA Band 6 data obtained for Himiko. It is motivated by a recent discovery of a bright millimeter emission line beyond their target, nearby merging galaxies VV114 (Tamura et al. 2014). Their spectral energy distribution (SED) analysis has shown that the detected line is likely a redshifted  $^{12}\text{CO}$  emission line from an X-ray bright galaxy at  $z = 2.467$ , demonstrating that deep interferometric observations with high angular resolution can fortuitously detect emission lines not only from their main targets (Swinbank et al. 2012) but also from sources other than the targets (see also, Kanekar et al. 2013).

The outline of this paper is as follows. After describing the ALMA observations and data reduction in Section 2, we perform source extractions and carry out simulations to derive the number counts of SMGs in Section 3. In Section 4, after we construct the number counts, we compare them with the previous observational results and model predictions, and estimate the contributions from the resolved sources to the EBL at 1.2 mm. In the next section, we present the results of our counts-in-cells analysis for faint SMGs. In Section 6, we report detections of serendipitous submillimeter emission lines in our ALMA data. A summary is presented in Section 7.

Throughout this paper, we assume a flat universe with  $\Omega_{\text{m}} = 0.3$ ,  $\Omega_{\Lambda} = 0.7$ ,  $n_{\text{s}} = 1$ ,  $\sigma_8 = 0.8$ , and  $H_0 = 70 \text{ km s}^{-1} \text{ Mpc}^{-1}$ . We use magnitudes in the AB system (Oke & Gunn 1983). Following the method by Hatsukade et al. (2013), we scale the flux density of a source observed at a wavelength different from 1.2 mm to the flux density at 1.2 mm by using a modified black-body with typical values for SMGs as noted above. For the data that we analyze in this paper, we adopt the flux density ratios summarized in Table 1. For the other data, we use  $S_{1.2\text{mm}}/S_{870\mu\text{m}} = 0.43$ ,  $S_{1.2\text{mm}}/S_{1.1\text{mm}} = 0.79$ , and  $S_{1.2\text{mm}}/S_{1.3\text{mm}} = 1.25$ .

## 2. ALMA DATA

We analyze continuum maps at around 1 mm with high sensitivities and high angular resolutions, obtained in ALMA cycle 0 and cycle 1 observations. In this section, we introduce the ALMA Band 6 data taken by our programs, and the other deep ALMA Band 6/Band 7 data that we use.

### 2.1. Our Data

TABLE 1  
SURVEY FIELDS

Map	Target	$\lambda_{\text{obs}}$ (mm) (1)	$\nu_{\text{obs}}$ (GHz) (2)	$S_{1.2\text{mm}}/S_{\text{obs}}$ (3)	References (4)
1	Himiko	1.16	259	0.90	(a)
2	NB921-N-79144	1.22	245	1.05	(b)
3	LESS J033229.4–275619	1.21	247	1.03	(c)
4	CFHQS J0210–0456	1.20	249	1.00	(d)
5	CFHQS J2329–0301	1.20	250	1.00	(d)
6	ULAS J131911.29+095051.4	1.16	258	0.91	(e)
7	SDSS J104433.04–012502.2	1.04	288	0.68	(e)
8	SDSS J012958.51–003539.7	1.04	288	0.68	(e)
9	SDSS J231038.88+185519.7	1.14	263	0.87	(e)
10	SDSS J205406.49–000514.8	1.15	261	0.89	(e)

NOTES. — (1) Observed wavelength. (2) Observed frequency. (3) Ratio of the flux density at 1.2 mm,  $S_{1.2\text{mm}}$ , to the observed flux density,  $S_{\text{obs}}$ , on the assumption of a modified blackbody with typical values for SMGs. (4) (a) Ouchi et al. (2013); (b) R. Momose et al. in preparation; (c) Nagao et al. (2012); (d) Willott et al. (2013); (e) Wang et al. (2013).

We use the ALMA data originally obtained by Ouchi et al. (2013), who targeted an extremely luminous Ly $\alpha$  blob at  $z = 6.595$ , Himiko. Deep ALMA Band 6 observations were carried out in 2012 July 15, 18, 28, and 31 with a 16 12-m antenna array under the extended configuration of 36 – 400 m baseline. To detect the redshifted [CII]158  $\mu\text{m}$  line and simultaneously the dust continuum emission, they adopted four spectral windows with a bandwidth of 1875 MHz. The central frequency of the four spectral bands is 250.24 GHz, 252.11 GHz, 265.90 GHz, and 267.78 GHz. They used 3c454.3 and J0423–013 for bandpass calibrators and J0217+017 for a phase calibrator. Neptune and Callisto were observed as a flux calibrator. The total on-source integration time was 3.17 hours.

We also use newly obtained ALMA Band 6 data (PI: R. Momose) taken for a spectroscopically confirmed Ly $\alpha$  emitter (LAE) at  $z = 6.511$ , NB921-N-79144 (Ouchi et al. 2010). They carried out deep ALMA Band 6 observations in 2013 June 18 and 19 with 23 antennas. They used four spectral windows, one with a bandwidth of 1875 MHz and three with 2000 MHz, to detect the redshifted [CII] line and dust continuum. The central frequency of the four spectral bands is 237.62 GHz, 240.42 GHz, 255.42 GHz, and 253.05 GHz. J0238+166 and J2258–279 were observed as a flux calibrator. The bandpass and phase were calibrated with J0204–1701 and J0215–0222, respectively. The total on-source integration time was 1.22 hours.

The data were reduced with the Common Astronomy Software Applications (CASA; McMullin et al. 2007) package in a standard manner. Hereafter, the maps reduced from the data taken by Ouchi et al. (2013) and R. Momose et al. in preparation are referred to as Map 1 and Map 2, respectively. The final synthesized beam sizes of the maps are  $\sim 0''.6 - 0''.8$ . The  $1\sigma$  noise of Map 1 (Map 2) is 17 (52)  $\mu\text{Jy beam}^{-1}$  and is almost constant in the map uncorrected for the primary beam attenuation. Further details of the ALMA observations and sensitivities are summarized in Ouchi et al. (2013) and will be presented in R. Momose et al. in preparation. In what follows, we use the ALMA continuum maps within the primary beam model.

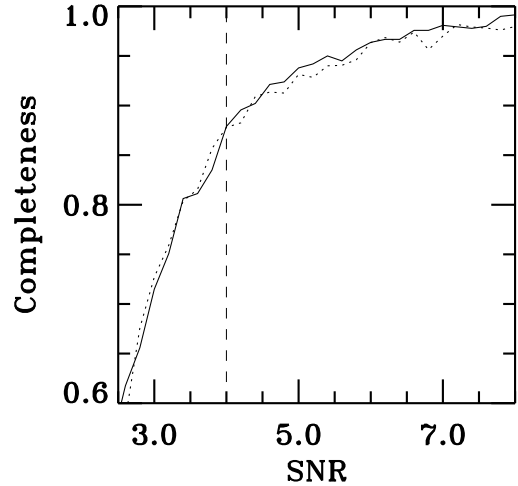


FIG. 1.— Completeness as a function of SNR estimated by Monte Carlo simulations. The solid curve and the dotted curve are the results of the simulations for Map 1 and Map 2, respectively. The vertical dashed line corresponds to the detection threshold we adopt.

## 2.2. Archival Data

To increase the number of SMGs for deriving the number counts, we take advantage of archival ALMA data that have been already public on the ALMA science archive.<sup>4</sup> We include the ALMA Band 6 and Band 7 data with relatively long integration time taken by Nagao et al. (2012), Willott et al. (2013), and Wang et al. (2013).

Their observations were conducted for spectroscopically confirmed quasars at  $z \sim 5 - 6$ . The number of the archival maps is eight in total: one from Nagao et al. (2012), two from Willott et al. (2013), and five from Wang et al. (2013). Their targets and the central wavelengths of the continuum observations are summarized in Table 1. The final synthesized beam sizes of the maps are  $\sim 0''.6 - 1''.5$ . The  $1\sigma$  noises of the maps uncorrected for primary beam attenuations are  $\simeq 21 - 88 \mu\text{Jy beam}^{-1}$ . For each map, we use the area contained in the primary beam.

<sup>4</sup> <https://almascience.nrao.edu/aq/>

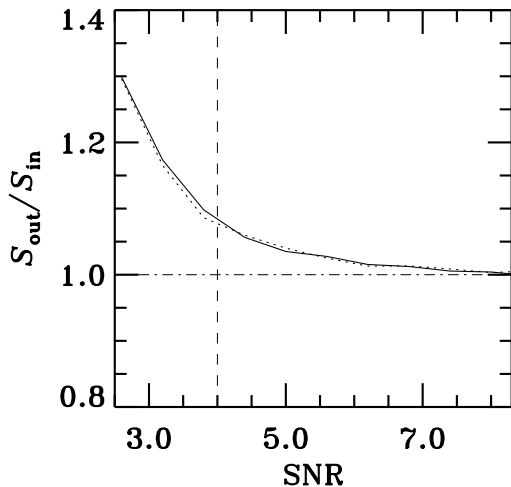


FIG. 2.— Flux boosting as a function of SNR estimated by Monte Carlo simulations. The solid curve and the dotted curve are the results of the simulations for Map1 and Map 2, respectively. The horizontal dot-dashed line corresponds to  $S_{\text{out}} = S_{\text{in}}$ . The vertical dashed line shows the source detection threshold,  $\text{SNR} = 4$ .

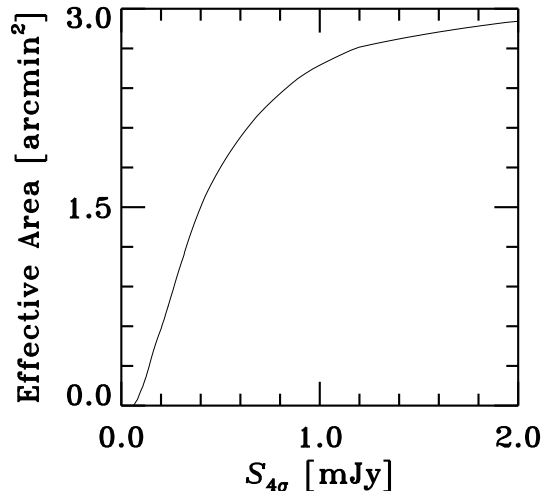


FIG. 3.— Total effective area of the ALMA maps analyzed in this study as a function of flux density, where a source with the flux density is detected at  $> 4\sigma$  in the primary beam corrected map.

### 3. DATA ANALYSIS

In this section, we analyze the deep ALMA maps for the 10 separate fields to derive the 1.2 mm number counts of SMGs, basically following the method described in Hatsukade et al. (2013).

#### 3.1. Source Extraction

Source extractions are conducted on the ALMA maps before primary beam correction with SExtractor version 2.5 (Bertin & Arnouts 1996). A collection of at least six contiguous pixels above the  $1.8\sigma$  sky noise are identified as an object. We do not extract the targeted sources.

Since the limit on significance levels for the source extractions is not high, some of our detections could be spurious caused by noise confusions. To estimate the fraction of spurious source detections, we use a negative ALMA map, i.e., a map multiplied by  $-1$ . The num-

TABLE 2  
DIFFERENTIAL NUMBER COUNTS OF SMGS AT  
1.2MM

$S$ (mJy)	$\log(n)$ ( $[\Delta \log S = 1]^{-1} \text{deg}^{-2}$ )
This Study	
0.13	$4.88^{+0.84}_{-1.04}$
0.20	$4.69^{+0.84}_{-1.04}$
0.32	$4.63^{+0.58}_{-0.65}$
0.50	$4.33^{+0.68}_{-0.79}$
0.79	$3.82^{+0.84}_{-1.04}$
Hodge et al. (2013) and Karim et al. (2013)	
1.26	$2.68^{+0.24}_{-0.24}$
2.00	$2.97^{+0.16}_{-0.16}$
3.16	$2.74^{+0.21}_{-0.22}$
5.01	$1.40^{+1.19}_{-1.75}$

ber of spurious sources is obtained by extracting sources from the negative map in the same manner as that for the positive map. We find that the angular distribution of the spurious sources is almost uniform. The number of spurious sources is less than that of positive sources at signal-to-noise ratio ( $\text{SNR}$ )  $\gtrsim 3.5$ , which is consistent with the results of Hatsukade et al. (2013).

We limit the catalogs to objects whose SNR is higher than 4.0. In the 10 ALMA maps, we detect thirteen SMGs with SNRs of 4.1 – 6.1. All the SMGs are point sources or at most marginally resolved. We find that two SMGs found in Maps 1 and 2 have possible counterparts in the Subaru optical images (Furusawa et al. 2008) and the *Hubble Space Telescope* (*HST*) near-infrared images (Ouchi et al. 2013). Their detailed properties will be presented elsewhere. Note that an SMG detected in Map 5 has already been identified by Willott et al. (2013) as a blue galaxy at a moderate redshift (see their Figure 1).

#### 3.2. Completeness and Flux Boosting

We calculate the detection completeness, which is the expected rate at which a source is detected in a map, to estimate the effects of noise fluctuations on source extractions. Since the source extractions are performed in the maps uncorrected for primary beam attenuation, the completeness estimations are conducted in the maps before primary beam corrections as well. We put a flux-scaled synthesized beam into a map as an artificial source. Since the noise level is almost constant in each map, the input position of an artificial source is randomly chosen in the map. We put artificial sources whose SNRs are in the range of 2–9. We perform source extractions in the same manner as that conducted for the actual maps (Section 3.1). From the fraction of recovered objects, we compute the completeness as a function of SNR (Figure 1).

It has been reported that SNR limited source catalogs carry a selection bias from an overabundance of sources whose apparent fluxes are positively enhanced by noises (e.g., Hogg & Turner 1998; Scott et al. 2002). From the simulations for estimating the detection completenesses, we also address this flux boosting issue. The results of our simulations are shown in Figure 2, where we present the ratio of the extracted flux densities  $S_{\text{out}}$  to the input flux densities  $S_{\text{in}}$  as a function of SNR. The systematic



differences between the output and input flux densities are less than only 10% at  $\text{SNR} > 4$ . We divide the observed flux density of a detected source by the average ratio at the SNR of the source to obtain the de-boosted flux density.

#### 4. NUMBER COUNTS AT 1.2 MM

##### 4.1. Derivation of Number Counts

By using the serendipitously discovered SMGs with SNRs of  $> 4$ , we derive the differential number counts of SMGs at 1.2 mm. First, we estimate the effective area as a function of flux density (corrected for primary beam attenuation), since the primary beam response in a map depends on the distance from the center of the map. The derived effective area is shown in Figure 3 as a function of  $4\sigma$  flux density,  $S_{4\sigma}$ .

Using the results of our simulations described in Section 3, we correct for the contamination of spurious sources and the effect of the incompleteness. A contribution from a detected source with an intrinsic flux density of  $S$  to the number count,  $\xi(S)$ , is measured as

$$\xi(S) = \frac{1 - f_c(S)}{C(S)A_{\text{eff}}(S)} \quad (1)$$

where  $f_c$  is the contamination fraction,  $C$  is the completeness, and  $A_{\text{eff}}$  is the effective survey area. Then, we calculate a sum of the contributions,  $n(S) = \sum \xi(S)/\Delta \log S$  in each logarithmic flux density bin  $\log S \pm (1/2)\Delta \log S$ , where  $\Delta \log S = 0.2$ , to obtain a logarithmic, differential number count. The  $1\sigma$  uncertainties are calculated from Poisson confidence limits (Gehrels 1986). The derived number counts are summarized in Table 2.

##### 4.2. Comparison with Previous Studies

The number counts of the faint ( $0.1 - 1$  mJy, or  $\text{SFR}_{\text{IR}} \sim 30 - 300 M_{\odot} \text{ yr}^{-1}$ ) SMGs revealed by the deep and high angular resolution ALMA observations are presented in Figure 4. The obscured SFR derived from the 1.2 mm flux density by the same method as described in Section 1 is given on the upper  $x$ -axis. Since the total survey area of our data is not large, we find no source brighter than 1 mJy. For the number counts of bright ( $> 1$  mJy) SMGs, we make use of the source catalog obtained from the recent follow-up observations of bright LABOCA sources with ALMA (Hodge et al. 2013; Karim et al. 2013). We use 91 sources whose SNRs are higher than 4.0 in Table 3 and Table 4 of Hodge et al. (2013). Considering the completeness and spurious detection rates estimated by Karim et al. (2013), we derive the number counts in the flux density range of  $\simeq 1 - 5$  mJy, which are presented in Table 2 as well. We also construct the differential number counts using the source catalog of Hatsukade et al. (2013) considering their estimates on the contamination rate of spurious sources, the incompleteness, and the effective survey area for each source.

From Figure 4, we find that the differential number counts increase with decreasing flux density down to 0.1 mJy. We also find that the slope of the logarithmic number counts at sub-mJy flux densities is relatively small. The number counts increase by more than three orders of magnitude from 10 mJy to 1 mJy, while they increase by

TABLE 3  
BEST-FIT PARAMETERS OF PARAMETRIC FITS  
TO THE DIFFERENTIAL NUMBER COUNTS OF SMGS

Function	$S_*$ (mJy)	$\phi_*$ ( $10^2 \text{ deg}^{-2}$ )	$\alpha$	$\beta$	$\chi_r^{2\dagger}$
Schechter	$2.4^{+2.6}_{-1.0}$	$8.5^{+21.4}_{-7.1}$	$-2.5^{+0.3}_{-0.3}$	—	1.6
DPL	$4.8^{+0.0}_{-0.8}$	$1.0^{+0.5}_{-0.0}$	$2.8^{+0.1}_{-0.1}$	$46^{+40}_{-36}$	1.5

$\dagger$  Reduced  $\chi^2$ .

only about an order of magnitude from 1 mJy to 0.1 mJy. This indicates that the slope of the number counts of the faint SMGs is smaller than that of the bright SMGs.

Figure 4 shows that the differential number counts of Hatsukade et al. (2013) probe similarly faint flux densities, and are broadly consistent with our results within the  $1\sigma$  uncertainties. It should be noted that they observed a continuous small field, while we compile the results of the 10 independent fields. The effect of field-to-field variations on our measurements of number counts is expected to be smaller than that on the results of Hatsukade et al. (2013).

At bright flux densities around 4 mJy, which corresponds to an obscured SFR of  $\sim 1000 M_{\odot} \text{ yr}^{-1}$ , we confirm that the differential number counts drop off, as Karim et al. (2013) have already pointed out. The lack of large numbers of the bright SMGs implies that the obscured SFRs of dusty galaxies have a natural limit, which may be due to feedback processes by active galactic nuclei (e.g., Croton et al. 2006; Bower et al. 2006) and/or supernovae (e.g., Springel & Hernquist 2003), but also due to shortage of gas supply for star formation (Karim et al. 2013; Hayward et al. 2013). Note that the number counts at the bright end are derived only from the observations in the Extended Chandra Deep Field-South (ECDF-S), which could be affected by cosmic variance. This issue should be addressed by further observations of other large fields with ALMA.

Figure 4 also presents the results from single-dish AzTEC observations at 1.1 mm. We confirm that the single-dish observational results significantly overestimate the number counts at the bright end likely due to the poor angular resolutions (see also, Karim et al. 2013). Observations with high angular resolution are required for avoiding bias due to source confusions.

Next we compare the observed number counts to theoretical predictions. In Figure 4, the number counts predicted by Shimizu et al. (2012) are shown. They have performed cosmological hydrodynamic simulations with GADGET-3, implementing a simple dust absorption model and modified blackbody emission for the IR SEDs of galaxies. In their calculations, they have considered simulated galaxies with dark halo masses of  $M_{\text{DH}} > 10^{10} M_{\odot}$ . Figure 4 indicates that their predictions agree well with our observational results down to  $\simeq 0.1$  mJy, and roughly reproduce the results at brighter flux densities of  $\simeq 1 - 3$  mJy taken from the literature. This implies that the number counts of the SMGs with flux densities larger than 0.1 mJy can be well explained by the abundance of galaxies with dark halo masses of  $> 10^{10} M_{\odot}$ . In Figure 4, the model predictions provided by Hayward et al. (2013) are presented as well. They have adopted a hybrid approach by combining a

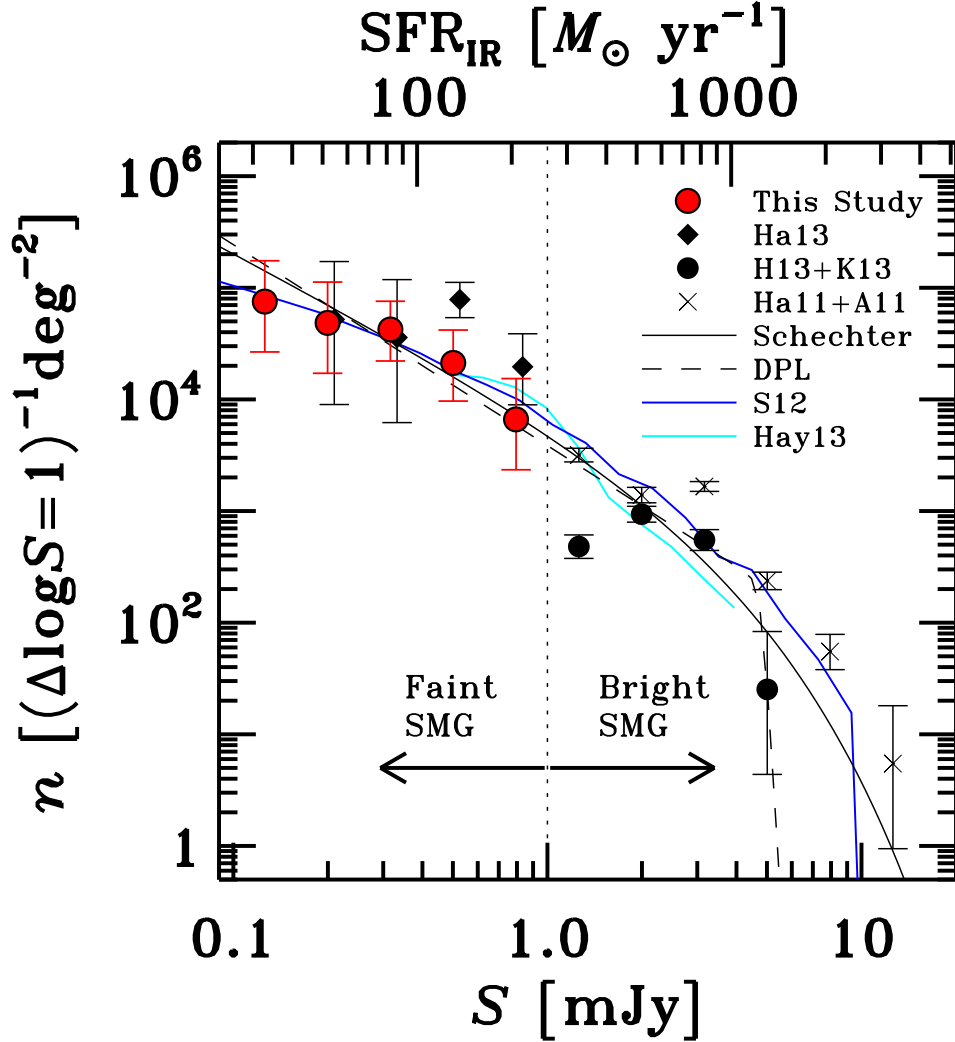


FIG. 4.— Differential number counts based on the results of ALMA observations. The number density of SMGs per  $\Delta \log S = 1$  per unit square degree is plotted against flux density  $S$  with corresponding  $\text{SFR}_{\text{IR}}$  on the upper  $x$ -axis. The red filled circles are the number counts derived from the faint SMGs found in this study. The black filled diamonds are the number counts estimated by using the source catalog of Hatsukade et al. (2013). Their flux densities have been shifted by  $+0.05$  logarithmic units for clarity. The black filled circles are calculated based on the catalog of bright SMGs obtained from the ALMA Band 7 observations (Hodge et al. 2013; Karim et al. 2013). The crosses are the number counts of bright SMGs detected with ASTE AzTEC at 1.1 mm (Hatsukade et al. 2011; Aretxaga et al. 2011). The solid curve shows the best-fit Schechter function and the dashed curve is the best-fit DPL function. The blue curve shows the model predictions for the number counts based on cosmological hydrodynamic simulations with GADGET-3 (Shimizu et al. 2012). The cyan curve corresponds to the model predictions calculated by combining a semi-empirical model with 3D hydrodynamical simulations and dust radiative transfer (Hayward et al. 2013).

semi-empirical model with 3D hydrodynamical simulations and 3D dust radiative transfer calculations. Their model predictions for the number counts are also broadly consistent with our observational results at  $\simeq 0.5$ – $1$  mJy and those at brighter flux densities in the literature.

#### 4.3. Contributions to the Extragalactic Background Light

We have constructed the 1.2 mm number counts of SMGs based on the results of the multifield deep ALMA observations, which reduce biases due to field-to-field variations and source confusions. Using the improved number counts, we refine the estimates on the integrated flux density from resolved sources and their contributions to the EBL.

The integrated flux density from sources resolved into discrete objects can be calculated by integrating the

product of the flux density and the number counts down to a flux density limit. In advance of integrating contributions from the resolved sources, we characterize the differential number counts using the following two functions often used in the literature.

One form is a Schechter function (Schechter 1976),

$$\phi(S)dS = \phi_* \left( \frac{S}{S_*} \right)^\alpha \exp \left( -\frac{S}{S_*} \right) d \left( \frac{S}{S_*} \right), \quad (2)$$

where  $\phi_*$ ,  $S_*$ , and  $\alpha$  are the normalization, the characteristic flux density, and the faint-end slope, respectively. This functional form is motivated by the relationship between millimeter flux density and rest-frame FIR luminosity, which is nearly constant at high redshifts (Blain et al. 2002; Coppin et al. 2006). We define the logarithmic Schechter function  $n(S)$  as  $n(S)d(\log S) =$

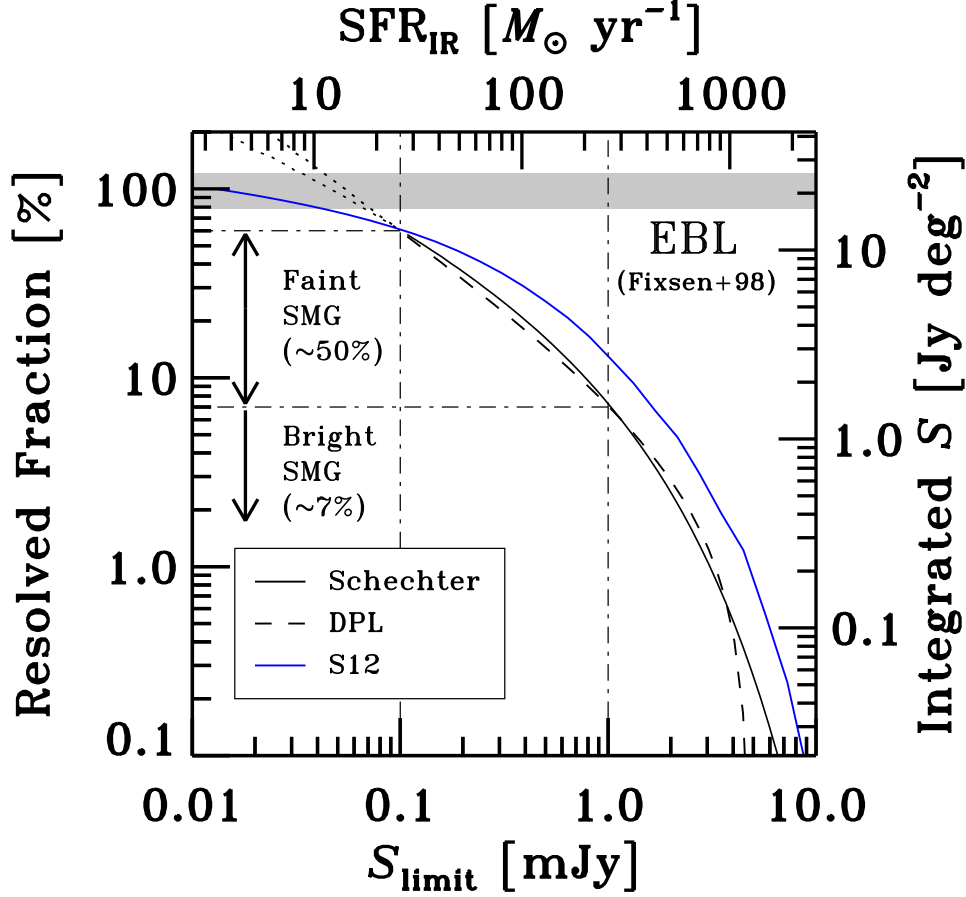


FIG. 5.— Fraction of resolved background light as a function of flux density limit at 1.2 mm,  $S_{\text{limit}}$  with corresponding  $\text{SFR}_{\text{IR}}$  on the upper axis. On the right axis, the absolute value of the integrated flux density,  $\int_{S_{\text{limit}}}^{\infty} S\phi(S)dS$ , is shown. The black solid curve and the dashed curve correspond to the cases of our best-fit Schechter function and DPL function, respectively. The dotted curves represent simple extrapolations of the best-fit functions down to fainter  $S_{\text{lim}}$  than our survey limit. The blue curve is calculated from the predicted number counts of Shimizu et al. (2012). The gray hatched region is the extragalactic background light measured by the *COBE* satellite (Fixsen et al. 1998).

$\phi(S)dS$ , i.e.,

$$n(S) = (\ln 10) \phi_* 10^{(\alpha+1)(\log S - \log S_*)} \times \exp\left(-10^{(\log S - \log S_*)}\right), \quad (3)$$

and fit it to the differential number counts derived from the results of our observations as well as the previous observations. In the fitting, we take into account the following results: the number counts of the faint (0.1 – 1.0 mJy) SMGs presented in this paper, the number counts of the faint SMGs at  $\simeq 0.2 - 1.0$  mJy constructed from the source catalog of Hatsukade et al. (2013), and the number counts of the bright ( $> 1$  mJy) SMGs derived from the source catalog of Hodge et al. (2013) (see also, Karim et al. 2013). Note that we do not use the data point at  $\simeq 1.2$  mJy, since it seems to be incomplete. Varying the three parameters, we search for the best-fitting set of  $(\phi_*, S_*, \alpha)$  that minimizes  $\chi^2$ . The best-fit parameters are shown in Table 3, and the best-fit Schechter function is plotted in Figure 4.

The other form is a double power law (DPL) function (e.g., Scott et al. 2002; Coppin et al. 2006):

$$\phi(S) = \frac{\phi_*}{S_*} \left[ \left( \frac{S}{S_*} \right)^\alpha + \left( \frac{S}{S_*} \right)^\beta \right]^{-1}, \quad (4)$$

where the definition of  $\phi_*$ ,  $S_*$ , and  $\alpha$  are the same as those in equation (2), and  $\beta$  is the bright-end slope. The logarithmic DPL function  $n(S)$  is defined as  $n(S)d(\log S) = \phi(S)dS$ , i.e.,

$$n(S) = \frac{(\ln 10) \phi_*}{10^{(\alpha-1)(\log S - \log S_*)} + 10^{(\beta-1)(\log S - \log S_*)}}. \quad (5)$$

Varying the four parameters, we search for the best-fitting DPL function that minimizes  $\chi^2$ . Table 3 shows the best-fit set of the parameters. Figure 4 shows the best-fit DPL function as well.

Using the best-fit parameter sets, we calculate integrated flux densities,  $\int_{S_{\text{lim}}}^{\infty} S\phi(S)dS$  down to a lower limit of flux density,  $S_{\text{lim}}$ . Figure 5 shows the integrated flux densities on the right axis, as a function of  $S_{\text{lim}}$ . The integrated flux density down to the survey limit,  $S_{\text{lim}} = 0.1$  mJy, is calculated to be  $\simeq 11 \text{ Jy deg}^{-2}$ , whichever of the two functional forms is adopted. Note that the EBL at 1.2 mm has been estimated to be  $21.1^{+4.4}_{-4.6} \text{ Jy deg}^{-2}$  based on the observations by the Far Infrared Absolute Spectrophotometer (FIRAS) aboard the *COBE* satellite (Fixsen et al. 1998).

On the left axis of Figure 5, we show the fraction of the contributions from the resolved sources to the total

EBL. We find that the faint ( $0.1 - 1$  mJy, or  $\text{SFR}_{\text{IR}} \sim 30 - 300 M_{\odot} \text{ yr}^{-1}$ ) SMGs contribute nearly a half of the EBL. Since the contributions from the bright SMGs are found to be less than 10%, the remaining half of the EBL is mostly contributed by very faint SMGs with flux densities of  $< 0.1$  mJy ( $\text{SFR}_{\text{IR}} \lesssim 30 M_{\odot} \text{ yr}^{-1}$ ). Although the resolved fraction of the EBL down to the survey limit is comparable to what Hatsukade et al. (2013) have reported, the effects of field-to-field variations are reduced in our estimates. Note that the resolved fraction is significantly higher than those reported in the previous single-dish surveys at 1 mm (e.g., Greve et al. 2004; Hatsukade et al. 2011). The higher sensitivities and higher resolutions of the ALMA maps enable us to push the survey limit down to the sub-mJy levels.

Interestingly, based on the theoretical prediction of Shimizu et al. (2012), the integrated flux density calculated with the predicted number counts appears to converge to the EBL at 0.01 mJy, which corresponds to  $\text{SFR}_{\text{IR}} \simeq 3 M_{\odot} \text{ yr}^{-1}$ . This indicates that the EBL would be mostly explained by SMGs with  $S = 0.01 - 10$  mJy. In this case, the contributions to the EBL from galaxies with obscured SFRs of  $< 3 M_{\odot} \text{ yr}^{-1}$  would be negligibly small. It is also inferred that, since the model predictions by Shimizu et al. (2012) have considered simulated galaxies with  $M_{\text{DH}} > 10^{10} M_{\odot}$ , the dark halo masses of SMGs would be larger than  $10^{10} M_{\odot}$  and the contributions to the EBL from small galaxies with  $M_{\text{DH}} < 10^{10} M_{\odot}$  would be negligible. This would be consistent with some theoretical studies that have suggested star formation quenching processes due to SNe feedback and/or UV radiation feedback work effectively in such small systems (e.g., Okamoto et al. 2010; Hasegawa & Semelin 2013).

##### 5. COUNTS-IN-CELLS OF FAINT SMGS

The number of the detected SMGs differs among the maps, part of which could be induced by cosmic variance. From the field-to-field scatter in their number counts, we estimate the galaxy bias of the faint SMGs. With a sample of fields, the galaxy bias can be estimated from (Adelberger et al. 1998; Robertson 2010)

$$b_g^2 \simeq \frac{\sigma_N^2 - \bar{N}}{\bar{N}^2 \sigma_V^2(z)}, \quad (6)$$

where  $\bar{N}$  is the mean of source number counts per field,  $\sigma_N^2$  is the dispersion that includes contributions from both cosmic and Poisson variance, and  $\sigma_V^2(z)$  is the matter variance averaged over many survey volume  $V$  (e.g., Mo & White 2002). To estimate an effective survey volume, we use a redshift distribution of SMGs obtained by follow-up spectroscopic observations (Chapman et al. 2005). The redshift distribution has a long tail within  $z = 1 - 4$ , and its mean is  $\langle z \rangle \simeq 2.5$ .

To calculate the mean and the dispersion of observed number counts per field, we need to set a flux density limit. This is because detection limits of flux density depend on positions in the maps due to primary beam attenuations. If we take a flux density limit of 0.25 mJy with an uncertainty of a factor of two in flux density measurements, we obtain a mean number of sources brighter than the flux density limit of 0.6, a variance  $\sigma_N^2$  of 0.84, and a matter root-mean-square (rms) fluctuation  $\sigma_V(z)$

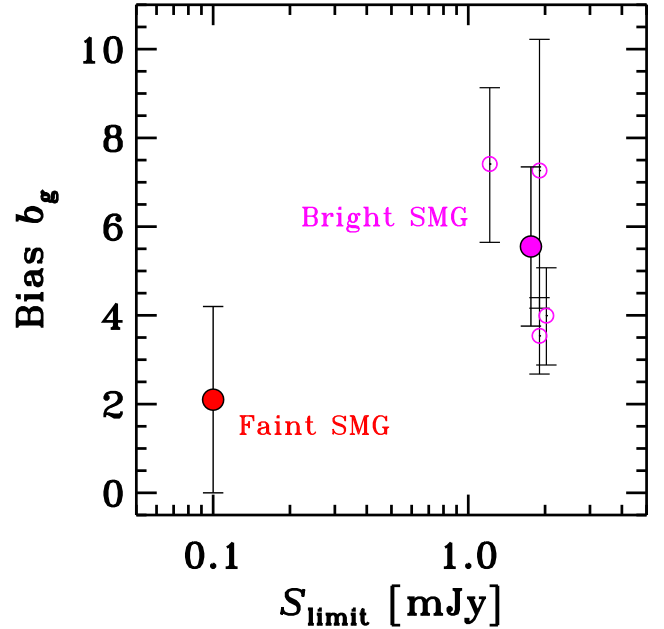


FIG. 6.— Bias of SMGs as a function of flux density limit,  $S_{\text{limit}}$ . The red circle represents the result of faint SMGs analyzed in this paper. The magenta circles indicate bright SMGs (Webb et al. 2003; Blain et al. 2004; Weiß et al. 2009; Hickox et al. 2012), and the filled magenta circle corresponds to their average.

of 0.39. The bias calculated for this galaxy abundance is  $b_g = 2.1 \pm 2.1$ . Note that if we take a flux density limit in the range of  $\simeq 0.15 - 0.3$  mJy with an uncertainty of a factor of 2–3, we obtain a bias in the range of  $\simeq 1.2 - 2.5$ , which is within the range of the  $1\sigma$  uncertainties.

Figure 6 shows our estimate on the galaxy bias of the faint SMGs as well as the previous estimates for bright ( $> 1$  mJy) SMGs (Webb et al. 2003; Blain et al. 2004; Weiß et al. 2009; Hickox et al. 2012) as a function of redshift. In the cases that galaxy biases are not presented and only the best-fit galaxy correlation functions are available in the literature, we calculate the galaxy bias from  $b_g = \sigma_{8,g}/\sigma_8(z)$ , where  $\sigma_8(z)$  is a matter fluctuation in spheres of comoving radius of  $8h^{-1}$  Mpc, and  $\sigma_{8,g}$  is a galaxy fluctuation, which is derived from (e.g., eq.[7.72] in Peebles 1993),

$$\sigma_{8,\text{gal}}^2 = \frac{72}{(3-\gamma)(4-\gamma)(6-\gamma)2^\gamma} \left( \frac{r_0}{8h^{-1}\text{Mpc}} \right)^\gamma, \quad (7)$$

where  $\gamma$  and  $r_0$  are the parameters of the galaxy correlation function. In Figure 6, Webb et al. (2003) and Blain et al. (2004) have derived correlation lengths of  $\simeq 11.5 h^{-1}$  Mpc and  $\simeq 6.9 h^{-1}$  Mpc for the bright SMGs, which correspond to biases of  $b_g = 7.4$  and 4.0, respectively. Similar results have been obtained for 870  $\mu\text{m}$  LABOCA sources (Weiß et al. 2009; Hickox et al. 2012). The average bias of the bright SMGs is calculated to be  $b_g = 5.6 \pm 1.8$ . The galaxy bias of the faint SMGs estimated in this study appears to be lower than those of the bright SMGs reported in the literature. This difference indicates the clustering segregation with the FIR luminosity in SMGs. Similar clustering segregations with respect to the rest-frame UV/optical luminosities have been also found in local galaxies (e.g., Norberg et al. 2002) and high-redshift



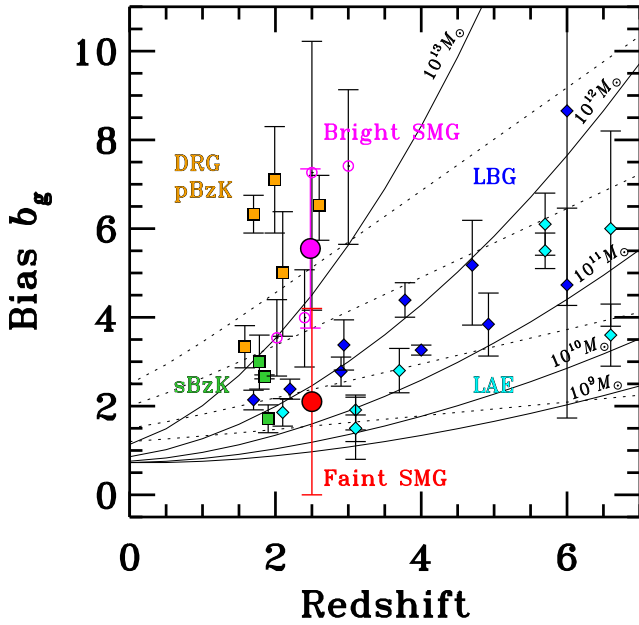


FIG. 7.— Bias of high redshift galaxies as a function of redshift. The red circle represents the result of faint SMGs analyzed in this paper. The open magenta circles indicate bright SMGs (Webb et al. 2003; Blain et al. 2004; Weiß et al. 2009; Hickox et al. 2012), and the filled magenta circle corresponds to their average. The blue diamonds represent LBGs and BX/BMs (Ouchi et al. 2004; Adelberger et al. 2005; Lee et al. 2006; Overzier et al. 2006). The cyan diamonds are LAEs (Gawiser et al. 2007; Ouchi et al. 2010; Guaita et al. 2010). The orange squares indicate DRGs and pBzKs (Grazian et al. 2006; Quadri et al. 2007; Blanc et al. 2008; Furusawa et al. 2011; Lin et al. 2012). The green squares are sBzKs (Hayashi et al. 2007; Blanc et al. 2008; Furusawa et al. 2011). The solid curves are bias of dark haloes with a mass of  $10^{13}$ ,  $10^{12}$ ,  $10^{11}$ ,  $10^{10}$ , and  $10^9 M_\odot$  from top to bottom, from Sheth & Tormen (1999) in the case of one-to-one correspondence between galaxies and dark haloes. The dotted curves indicate the passive evolution of galaxy biases governed by their motion within the gravitational potential, assuming no merging (Fry 1996).

galaxies (e.g., Giavalisco & Dickinson 2001; Ouchi et al. 2004; Lee et al. 2006; Hayashi et al. 2007; Yoshida et al. 2008).

It may be the case that some of the faint SMGs found in the archival data are physically related to the quasars at the center of the maps. However, since the redshift distribution of SMGs is substantially broad thanks to the negative  $K$ -correction (e.g., Chapman et al. 2005), the effective survey volume is much larger than the volume observed around the quasar. In fact, a faint SMG that is detected in Map 5 has already been identified at a much lower redshift than the target quasar (Willott et al. 2013), which indicates that at least the faint SMG has no physical relation to the quasar. In this study, we consider the faint SMGs detected in the archival maps have no relationship with the quasars, although we should keep in mind that the results might be biased by selecting the quasar fields. If this is the case, the galaxy bias of the faint SMGs would be smaller than our estimates.

Figure 7 shows the galaxy biases of the faint and bright SMGs as a function of redshift, as well as the previous estimates for a variety of galaxy populations:  $K$ -selected galaxies (Grazian et al. 2006; Hayashi et al. 2007; Quadri et al. 2007; Blanc et al. 2008; Furusawa et al. 2011; Lin et al. 2012) includ-

ing passively-evolving BzK galaxies (pBzKs), sBzKs and distant red galaxies (DRGs), and UV-selected galaxies (Ouchi et al. 2004; Adelberger et al. 2005; Overzier et al. 2006; Lee et al. 2006; Gawiser et al. 2007; Ouchi et al. 2010; Guaita et al. 2010) including BX/BM galaxies, LBGs and LAEs. At  $z \sim 2.5$ , the biases of DRGs and pBzKs appear to be higher than that of the faint SMGs, while  $K$ -selected galaxies with bluer UV colors (sBzKs) have similar bias values to the faint SMGs. The UV-selected galaxies at  $z \sim 2-3$  have similar galaxy biases to that of the faint SMGs as well. These results suggest that the dark halo masses of the faint SMGs are comparable to those of sBzKs and UV-selected galaxies at  $z \sim 2-3$ . This implies that some of the faint SMGs might be their FIR counterparts, which is also suggested by the results of the recent *Herschel* observations (Reddy et al. 2012; Lee et al. 2012; Decarli et al. 2014) as mentioned in Section 1.

Dark halo masses of galaxies can be estimated with bias values in the frame work of the  $\Lambda$ CDM model. The solid curves in Figure 7 indicate bias of dark haloes with a mass of  $10^{13}$ ,  $10^{12}$ ,  $10^{11}$ ,  $10^{10}$ , and  $10^9 M_\odot$  from top to bottom, predicted by the Sheth & Tormen (1999) model in the case of one-to-one correspondence between galaxies and dark haloes (see also Mo & White 2002). Applying the model predictions, we estimate the dark halo mass of the faint SMGs to be roughly  $10^{12} M_\odot$ , and its upper limit is  $\sim 10^{13} M_\odot$ . These values are consistent with what is inferred from the theoretical prediction of Shimizu et al. (2012) as noted in Section 4.3.

To discuss possible present-day descendants of the faint SMGs, we show evolutionary tracks of dark haloes for galaxy-conserving models, which assume that the motion of galaxies is purely caused by gravity, and that galaxy merging does not occur (Fry 1996). In this case, the dark haloes of the faint SMGs would evolve into local galaxies with  $b_g \lesssim 2$ . This yields an upper limit of the bias evolution, since in a more realistic extended Press-Schechter formalism (e.g., Lacey & Cole 1993), evolutionary tracks are on average below those of the galaxy-conserving models (e.g., Ichikawa et al. 2007). At the local Universe, the biases are in the range of  $\sim 2-4$  for galaxy clusters (Bahcall et al. 2003), about 2 for galaxy groups (Girardi et al. 2000), and in the range of  $\simeq 1.1-2.2$  for the SDSS galaxy sample (Zehavi et al. 2005, 2011). Our results imply that the faint SMGs could evolve into normal galaxies including Milky Way and might reside in galaxy groups at  $z = 0$ .

Since the number of the pencil-beam survey fields is small, our estimates on galaxy biases have relatively large uncertainties. However, our coarse counts-in-cells analysis demonstrates the potential of ALMA for investigating the galaxy biases of faint SMGs, which have been poorly understood. Our results will be improved after a large number of deep ALMA maps become available.

## 6. SERENDIPITOUS LINE DETECTIONS: EVIDENCE FOR A DARK SUBMILLIMETER EMITTER POPULATION?

In the previous sections, we have analyzed the velocity-integrated continuum maps and presented the number counts and the spatial clustering of the serendipitously discovered faint SMGs. In this section, we conduct a blind search for line emitters at  $\simeq 1.2$  mm in data cubes of Map 1 taken with the ALMA Band 6. The central

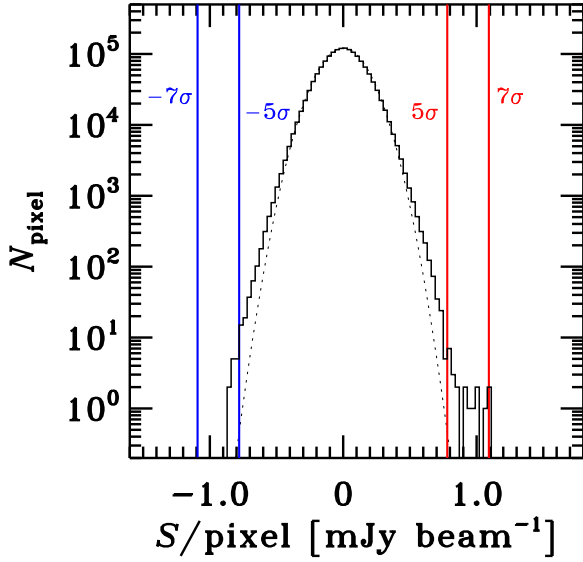


FIG. 8.— Histogram of flux density values (before primary beam correction) in the ALMA data cube with a frequency binning of  $\Delta v = 100 \text{ km s}^{-1}$ . The black solid line represents the values of the signal map in the primary beam. The dotted curve shows the Gaussian function with rms of  $\sigma \simeq 0.156 \text{ mJy beam}^{-1}$  that is determined by a  $\chi^2$  minimization fit to the histogram. The vertical blue lines correspond to  $-7\sigma$  and  $-5\sigma$  and the red lines are  $5\sigma$  and  $7\sigma$  from left to right.

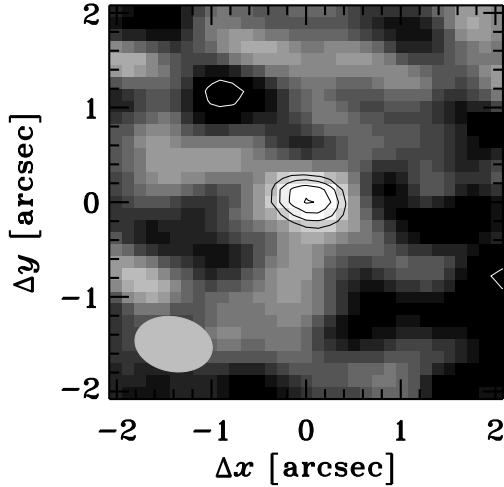


FIG. 9.— Emission-line map of a serendipitously detected line from a submillimeter emitter, SME-1, with a frequency binning of  $\Delta v = 100 \text{ km s}^{-1}$  and a spatial sampling of  $0.13 \text{ arcsec pixel}^{-1}$ . The black contours corresponds to  $4\sigma$ ,  $5\sigma$ ,  $6\sigma$  and  $7\sigma$  levels, and the white contour denotes  $-4\sigma$  level. The shape of the synthesized beam is given at the bottom-left corner.

frequency and the bandwidth of the data are  $250.24 \text{ GHz}$  and  $1875 \text{ MHz}$ , respectively.

We create a data cube with  $\Delta v = 100 \text{ km s}^{-1}$  binning, to search for serendipitous emission lines within the primary beam. Figure 8 presents a histogram of flux density values (uncorrected for the primary beam attenuation) in the data cube. The histogram is well represented by a Gaussian distribution with an rms of  $0.156 \text{ mJy beam}^{-1}$ . From the histogram and the emission-line maps in the data cube, we find that five sources show peak flux den-

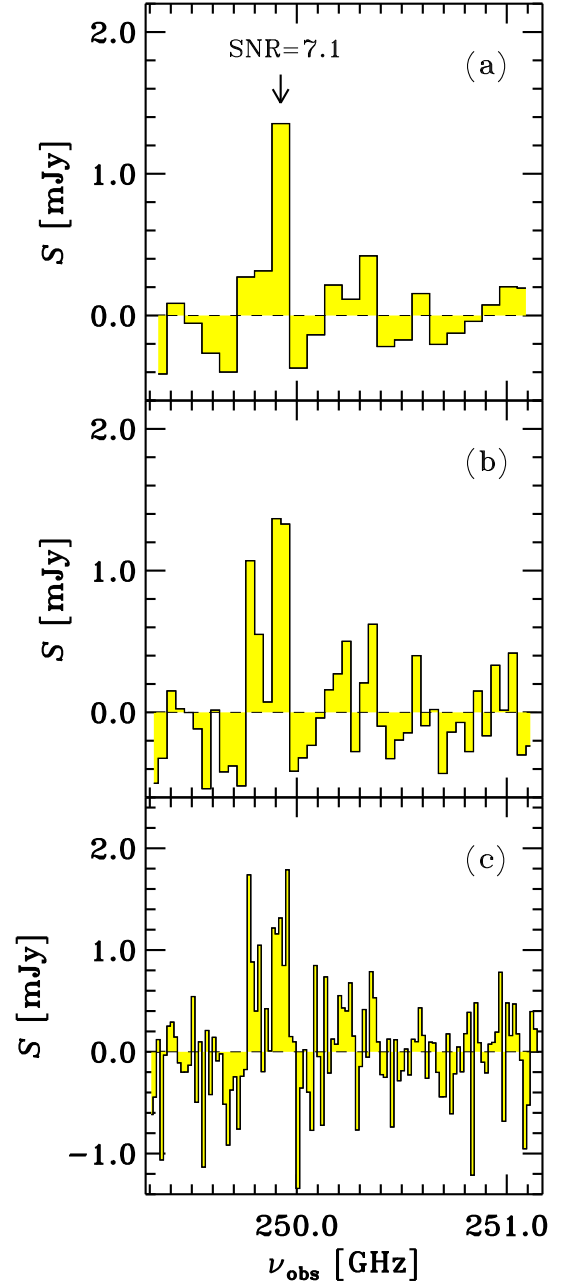


FIG. 10.— ALMA Band 6 spectra of SME-1 extracted at the position of the peak emission with frequency binnings of (a)  $\Delta v = 100 \text{ km s}^{-1}$ , (b)  $\Delta v = 50 \text{ km s}^{-1}$ , and (c)  $\Delta v = 20 \text{ km s}^{-1}$ . The flux densities are corrected for the primary beam attenuation. The SNR of the peak flux density in the spectrum of  $\Delta v = 100 \text{ km s}^{-1}$  is  $\simeq 7.1$ .

sities with SNRs of  $> 5$ . We also find that some negative sources show peak flux densities with SNRs in the range of  $-6$  to  $-5$ , and no negative source has a peak flux density with an SNR of  $< -7$ . This indicates that the spurious detection rates for sources with SNRs in the range of  $5 - 6$  are not negligible, while those for sources with SNRs  $> 7$  are substantially low.

Even if the five sources are not caused by statistical errors, they might be induced by unknown systematic noise effects in ALMA data cubes. If this is the case, we should be cautious in interpreting serendipitously detected sin-

TABLE 4  
LINE CANDIDATES FOR SME-1

Species	Transition	$\lambda_0$ ( $\mu\text{m}$ ) (1)	$\nu_0$ (GHz) (2)	$z$ (3)	$L$ ( $\text{erg s}^{-1}$ ) (4)	$L'$ ( $10^8 \text{ K km s}^{-1} \text{ pc}^2$ ) (5)	$L_{\text{IR}}^{(\text{exp})}$ ( $L_{\odot}$ ) (6)	$S^{(\text{exp})}$ ( $\mu\text{Jy}$ ) (7)
CO	$J = 3 \rightarrow 2$	867	345.80	0.384	$5.79 \times 10^{38}$	1.14	$1.9 \times 10^{10}$	32
CO	$J = 4 \rightarrow 3$	650.3	461.04	0.845	$3.90 \times 10^{39}$	3.24	$3.5 \times 10^{10}$	29
CO	$J = 5 \rightarrow 4$	520.2	576.27	1.31	$1.14 \times 10^{40}$	4.87	$3.8 \times 10^{10}$	27
CO	$J = 6 \rightarrow 5$	433.6	691.47	1.77	$2.41 \times 10^{40}$	5.94	$4.0 \times 10^{10}$	28
CO	$J = 7 \rightarrow 6$	371.7	806.65	2.23	$4.25 \times 10^{40}$	6.60	$5.2 \times 10^{10}$	37
CO	$J = 8 \rightarrow 7$	325.2	921.80	2.67	$6.72 \times 10^{40}$	6.98	$1.1 \times 10^{11}$	79
[C I]	$^3P_2 \rightarrow ^3P_1$	370.42	809.34	2.24	$4.30 \times 10^{40}$	6.61	$3.0 \times 10^{12}$	$2 \times 10^3$
[C I]	$^3P_1 \rightarrow ^3P_0$	609.14	492.16	0.969	$5.47 \times 10^{39}$	3.74	$1.4 \times 10^{11}$	$1.1 \times 10^2$
[C II]	$^3P_{3/2} \rightarrow ^3P_{1/2}$	157.74	1900.5	6.60	$5.64 \times 10^{41}$	6.69	$4.7 \times 10^{10}$	44
[O I]	$^3P_0 \rightarrow ^3P_1$	145.53	2060.1	7.24	$6.98 \times 10^{41}$	6.50	$6.5 \times 10^{12}$	$6 \times 10^3$
H <sub>2</sub> O	$1_{11} \rightarrow 0_{00}$	269.27	1113.34	3.46	$1.23 \times 10^{41}$	7.24	$1.3 \times 10^{13}$	$1 \times 10^4$
H <sub>2</sub> O	$2_{02} \rightarrow 1_{11}$	303.46	987.93	2.95	$8.42 \times 10^{40}$	7.11	$2.6 \times 10^{12}$	$2 \times 10^3$
H <sub>2</sub> O	$2_{11} \rightarrow 2_{02}$	398.64	752.03	2.01	$3.31 \times 10^{40}$	6.33	$1.2 \times 10^{12}$	$9 \times 10^2$
H <sub>2</sub> O	$2_{20} \rightarrow 2_{11}$	243.97	1228.79	3.92	$1.66 \times 10^{41}$	7.27	$4.9 \times 10^{12}$	$4 \times 10^3$
H <sub>2</sub> O	$3_{12} \rightarrow 3_{03}$	273.19	1097.37	3.39	$1.17 \times 10^{41}$	7.23	$4.1 \times 10^{12}$	$3 \times 10^3$
H <sub>2</sub> O	$3_{21} \rightarrow 3_{12}$	257.79	1162.91	3.65	$1.40 \times 10^{41}$	7.26	$3.6 \times 10^{12}$	$4 \times 10^3$
H <sub>2</sub> O	$4_{22} \rightarrow 4_{13}$	248.25	1207.64	3.83	$1.57 \times 10^{41}$	7.27	$1.4 \times 10^{13}$	$1 \times 10^4$
H <sub>2</sub> O	$5_{23} \rightarrow 5_{12}$	212.53	1410.62	4.64	$2.48 \times 10^{41}$	7.19	$7.4 \times 10^{12}$	$7 \times 10^3$
[O III]	$^3P_1 \rightarrow ^3P_0$	88.36	3393.0	12.6	$2.45 \times 10^{42}$	5.11	$> 5.8 \times 10^{10}$	$> 35$

NOTES. — (1) Rest-frame wavelength. For the species other than H<sub>2</sub>O, we refer to Table 1 of Carilli & Walter (2013). (2) Rest-frame frequency from Table 1 of Carilli & Walter (2013) and Table 1 of Yang et al. (2013). (3) Redshift. (4) Line luminosity. (5) Line luminosity calculated from eq.(8). (6) FIR luminosity estimated from the observed line flux. (7) Expected flux density at 259 GHz ( $\simeq 1.2 \text{ mm}$ ) from the estimated FIR luminosity, assuming a modified blackbody with typical values for SMGs.

gle emission lines in ALMA data cubes. If they are not induced by systematic noise, the detected lines are evidence for the existence of submillimeter/millimeter emitters (SMEs). The five SME candidates have the peak flux densities with SNRs of 7.1, 5.5, 5.3, 5.1, and 5.0. Hereafter, they are referred to as SME-1, 2, 3, 4, and 5, respectively. In what follows, we focus on SME-1, since the number of spurious sources with SNRs of  $> 7$  in the data cube is expected to be very low, only  $\sim 2 \times 10^{-6}$ . Note that we also conduct blind line emitter searches in data cubes with smaller binnings,  $\Delta v = 50$  and  $20 \text{ km s}^{-1}$ , but we detect no source as reliable as SME-1 with an SNR of  $> 7$ .

Figure 9 shows the spatial flux density distribution of SME-1 at  $\nu_{\text{obs}} = 249.9 \text{ GHz}$ . SME-1 has a point-source-like profile. The peak flux density corrected for the primary beam response is  $\simeq 1.4 \text{ mJy}$ .

In Figure 10, we plot spectra of SME-1 extracted at the position of the peak spectrum with three frequency binnings,  $\Delta v = 100, 50$ , and  $20 \text{ km s}^{-1}$  from top to bottom. The spectra with  $\Delta v = 50$ , and  $20 \text{ km s}^{-1}$  appear to show a two-component profile at  $\nu_{\text{obs}} = 249.8 - 249.9 \text{ GHz}$ . Two-component line profiles have been reported for CO emission lines from star-forming galaxies at  $z \sim 1.5 - 3$  (e.g., Coppin et al. 2007; Daddi et al. 2010; Tadaki et al. 2014) and SMGs at  $z \sim 1 - 5$  (e.g., Greve et al. 2005; Weiß et al. 2005a; Tacconi et al. 2006, 2008; Combes et al. 2012). The detected line might have an analogous, two-component profile. However, in the spectrum with  $\Delta v = 100 \text{ km s}^{-1}$ , one of the peaks at the lower frequency is smoothed out, which indicates that the SNR of the detected line is not high enough to conclude that the line has a two-component profile. Hereafter we consider the detected feature to be a single-peaked line. The flux of the detected line is calculated to be

$$(1.36 \pm 0.19) \times 10^{-1} \text{ Jy km s}^{-1}, \text{ or } (1.13 \pm 0.16) \times 10^{-18} \text{ erg s}^{-1} \text{ cm}^{-2}.$$

In our ALMA 1.2 mm continuum map (Map 1), we detect no continuum emission at the position of SME-1, as shown in the bottom-right panel of Figure 11. The  $3\sigma$  upper limit on the 1.2 mm continuum flux density of SME-1 is estimated to be  $64 \mu\text{Jy}$ . Such a faintness suggests that SME-1 would be a high-redshift source with an intrinsically strong FIR emission line.

Line candidates for SME-1 are summarized in Table 4. To examine the validity of the line candidates, first we roughly estimate the expected 1.2 mm continuum flux densities of SME-1 from the observed line flux and test whether they are consistent with the upper limit estimated from Map 1. In the cases of the CO lines, we obtain CO(3-2) line fluxes in units of  $\text{Jy km s}^{-1}$  by adopting the CO excitation ladder found in M82 (Weiß et al. 2005a, see also, Mao et al. 2000; Ward et al. 2003; Weiß et al. 2005b and Figure 4 of Carilli & Walter 2013).<sup>5</sup> Then, we derive CO(3-2) luminosities  $L'_{\text{CO}(3-2)}$  in units of  $\text{K km s}^{-1} \text{ pc}^2$  from the following equation (Solomon et al. 1992, see also the reviews of Solomon & Vanden Bout 2005 and Carilli & Walter 2013):

$$L' (\text{K km s}^{-1} \text{ pc}^2) = 3.25 \times 10^7 S_{\text{line}} \Delta v \frac{D_L^2(z)}{(1+z)^3 \nu_{\text{obs}}^2}, \quad (8)$$

where  $S_{\text{line}} \Delta v$  is the observed flux of the line in units of  $\text{Jy km s}^{-1}$ ,  $D_L(z)$  is the luminosity distance in Mpc,  $\nu_{\text{obs}}$  in GHz is the observed frequency. Then we estimate the expected FIR luminosities,  $L_{\text{IR}}^{(\text{exp})}$ , by using the

<sup>5</sup> As noted later, we confirm that adopting the CO excitation ladder of Milky Way does not change our conclusions.

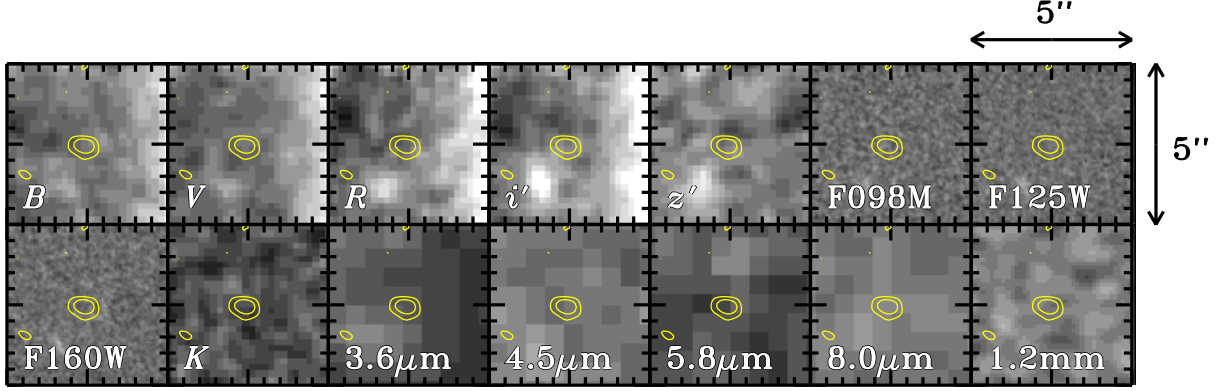


FIG. 11.—  $5'' \times 5''$  multiwavelength images of SME-1. Top panels show the images taken by the Subaru Suprime-Cam ( $B$ ,  $V$ ,  $R$ ,  $i'$ ,  $z'$ ) and the *HST* WFC3 (F098M, F125W). Bottom panels are the images taken by the *HST* WFC3 (F160W), the UKIRT WFCAM ( $K$ ), the *Spitzer* IRAC ( $3.6\mu\text{m}$ ,  $4.5\mu\text{m}$ ,  $5.8\mu\text{m}$ ,  $8.0\mu\text{m}$ ) and the ALMA Band 6 ( $1.2\text{mm}$ ). Contours correspond to the  $3\sigma$  and  $5\sigma$  levels of the detected line at  $249.9\text{ GHz}$ .

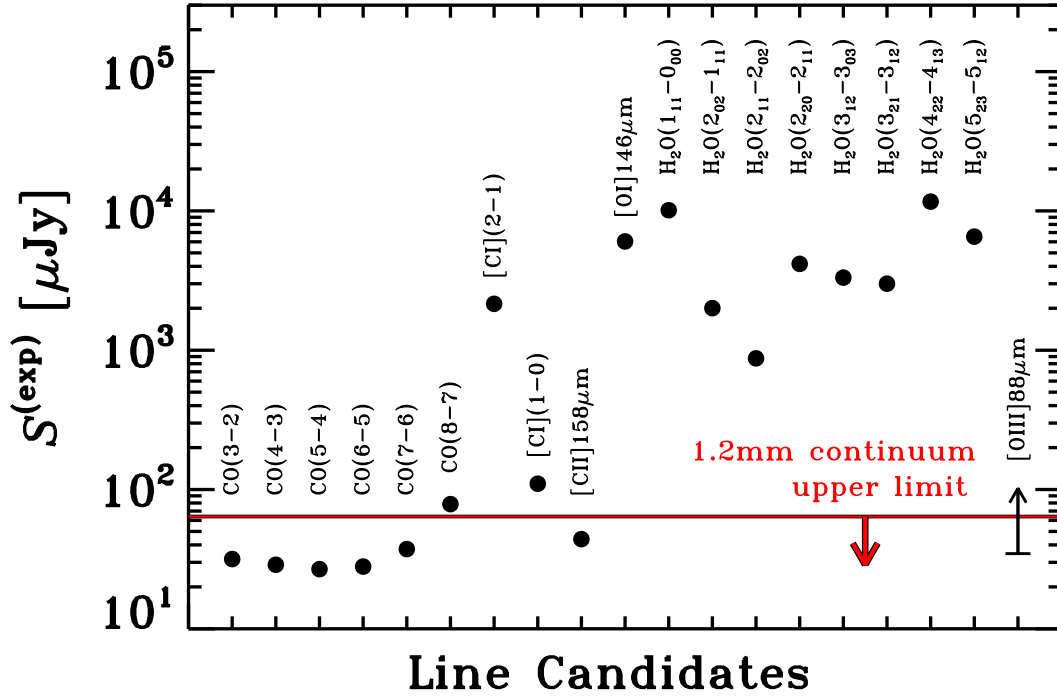


FIG. 12.— Expected  $1.2\text{ mm}$  continuum flux density of SME-1 for the line candidates. The red horizontal line represents the  $3\sigma$  upper limit of SME-1 estimated from Map 1.

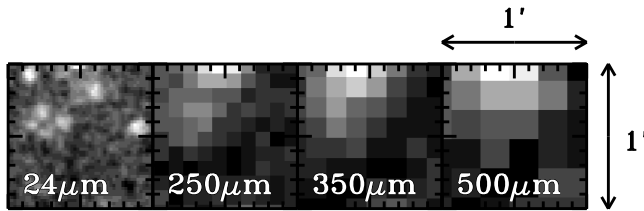


FIG. 13.— Mid- and far-infrared images of SME-1 taken by the *Spitzer* MIPS ( $24\mu\text{m}$ ) and the *Herschel* SPIRE ( $250\mu\text{m}$ ,  $350\mu\text{m}$ ,  $500\mu\text{m}$ ). SME-1 is located at the center. Because the size of each panel is  $1' \times 1'$ , which is 12 times larger than that in Figure 11, no contour of the detected line is shown.

relationship between the FIR luminosity and  $L'_{\text{CO}(3-2)}$  (Iono et al. 2009),  $\log L'_{\text{CO}(3-2)} = \alpha \log L_{\text{IR}} + \beta$ , where  $(\alpha, \beta) = (0.93, -1.50)$  and  $L'_{\text{CO}(3-2)}$  and  $L_{\text{IR}}$  are in units of  $\text{K km s}^{-1} \text{ pc}^2$  and  $L_{\odot}$ , respectively. From the estimated FIR luminosities, we calculate the expected continuum flux densities at  $\nu_{\text{obs}} = 259\text{ GHz}$ , which corresponds to  $1.2\text{ mm}$ , from (e.g., Ouchi et al. 1999)

$$S^{(\text{exp})} = \frac{(1+z)L_{\text{IR}}}{4\pi D_L^2(z)} \frac{\nu_0^{\beta_d} B(\nu_0, T_d)}{\int \nu^{\beta_d} B(\nu, T_d) d\nu}, \quad (9)$$

where  $B(\nu, T)$  is the Planck function, and  $\nu_0 = \nu_{\text{obs}}(1+z)$ . We use  $T_d = 35\text{ K}$  and  $\beta_d = 1.5$ , which are typical values of SMGs as noted in Section 1. Figure 12



presents the expected 1.2 mm continuum flux density for each line candidate. For the CO lines, the expected 1.2 mm continuum flux densities are broadly consistent with the upper limit estimated in our ALMA continuum map. The higher CO transitions do not seem plausible, since the expected continuum flux densities become larger as the rotational quantum number  $J$  increases.

If the detected line is [C $\text{I}$ ], the expected continuum flux densities are estimated to be 2 mJy and 0.1 mJy for [C $\text{I}$ ](2–1) and [C $\text{I}$ ](1–0), respectively, by adopting average ratios of  $L_{[\text{C}\text{I}](1-0)}/L_{[\text{C}\text{I}](2-1)} = 2.7$  and  $L_{[\text{C}\text{I}](1-0)}/L_{\text{IR}} \sim 10^{-5}$  (Walter et al. 2011). As shown in Figure 12, the estimated continuum flux density in the case of [C $\text{I}$ ](2–1) is more than an order of magnitude brighter than the upper limit of Map 1, while the estimated value for [C $\text{I}$ ](1–0) is consistent with the upper limit within a factor of two.

In the case that the detected line is [C $\text{II}$ ]158 $\mu\text{m}$ , we assume an average ratio of  $L_{[\text{C}\text{II}]} / L_{\text{IR}} \sim 3.1 \times 10^{-3}$  derived by Stacey et al. (2010) for star-forming galaxies at  $z = 1 - 2$ . The expected 1.2 mm continuum flux density is consistent with the upper limit estimated from the continuum map (Figure 12).

In the case of [O $\text{I}$ ]146 $\mu\text{m}$ , we adopt the relation between  $L_{\text{IR}}$  and the line luminosity,  $\log L_{\text{IR}} = \alpha + \beta \log L_{[\text{O}\text{I}]145\mu\text{m}}$ , where  $(\alpha, \beta) = (1.75, 1.34)$  obtained by Farrah et al. (2013). In this case, the expected 1.2 mm continuum flux density is two orders of magnitude brighter than the upper limit, suggesting that [O $\text{I}$ ]146 $\mu\text{m}$  is unlikely.

Recently, a series of detections of non-maser H $_2$ O emission lines have been reported for high-redshift galaxies (e.g., Omont et al. 2011; van der Werf et al. 2011; Lupu et al. 2012; Omont et al. 2013; Riechers et al. 2013). We estimate the expected 1.2 mm continuum flux densities in the cases that the detected line is H $_2$ O by using the relations between the H $_2$ O line luminosities and the FIR luminosity for starburst galaxies with  $L_{\text{IR}} \sim (1 - 300) \times 10^{10} L_{\odot}$  derived by Yang et al. (2013). As shown in Figure 12, the estimated 1.2 mm continuum flux densities are far brighter than the upper limit of the ALMA continuum data, which suggests that the detected line is not H $_2$ O.

For the line candidates of SME–1, we have investigated whether the expected 1.2 mm continuum flux densities from the observed line flux are consistent with the upper limit obtained from Map 1. We have found that the estimated 1.2 mm continuum flux densities are broadly consistent with the observed upper limit in the cases of the CO lines with the upper  $J$  levels of 3 – 8, [C $\text{I}$ ](1–0), and [C $\text{II}$ ]158 $\mu\text{m}$ . To further examine the validity of the lines, we search for possible counterparts in multiwavelength data. Figures 11 and 13 show SME–1 in the multiwavelength data: the Subaru Suprime-Cam optical  $BVRi'z'$  data (Furusawa et al. 2008), the UKIRT WFCAM near-infrared  $JHK$  data from the UKIDSS Ultra Deep Survey (UDS; Lawrence et al. 2007; Warren et al. 2007), the *HST* near-infrared data taken with the WFC3 F098M, F125W, and F160W filters (Ouchi et al. 2013) to which the data obtained by the Cosmic Assembly Near-IR Deep Extragalactic Legacy Survey (CANDELS; Grogin et al. 2011; Koekemoer et al. 2011) are added, the *Spitzer* IRAC 3.6 $\mu\text{m}$  and 4.5 $\mu\text{m}$  data (SEDS; Ashby et al. 2013)

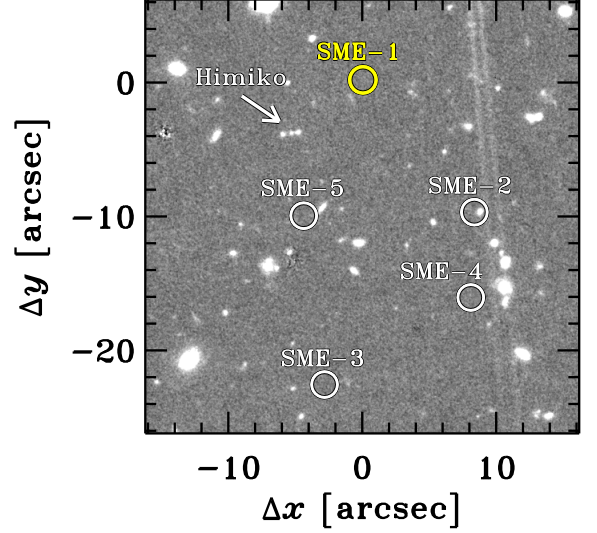


FIG. 14.— *HST* WFC3 F125W image of the SME candidates. The positions of the SME candidates and Himiko clumps are marked with circles and an arrow, respectively. To mark their positions, we use the CANDELS UDS astrometry, although Ouchi et al. (2009) have used the astrometry of the SXDS version 1.0 catalog.

as well as the 5.8 $\mu\text{m}$  and 8.0 $\mu\text{m}$ , and MIPS 24 $\mu\text{m}$  images (SpUDS; PI: J. Dunlop), and the *Herschel* SPIRE 250 $\mu\text{m}$ , 350 $\mu\text{m}$ , and 500 $\mu\text{m}$  data (HerMES; Oliver et al. 2012). However, we find no detectable source at the position of SME–1 in the multiwavelength images. In addition, SME–1 has no counterpart in the *Galaxy Evolution Explorer* (*GALEX*) FUV/NUV data (Nakajima et al. 2012) and the *XMM-Newton* data (Ueda et al. 2008). The  $3\sigma$  upper limits on the flux densities of SME–1 at wavelengths from the optical to 1.2 mm are summarized in Table 5. We also confirm that the other SME candidates (SME–2 to SME–5) have no counterpart in the multiwavelength data. Figure 14 shows a cutout of the WFC3 F125W image with the locations of the SME candidates.

Next, taking advantage of the upper limits estimated from the multiwavelength observations, we discuss what the detected line of SME–1 is. Figure 15 shows the multiwavelength SED of SME–1, together with the SED templates of dusty starbursts (Arp220 and M82) and spiral galaxies (M51 and NGC 6946) taken from Silva et al. (1998). The SED templates are normalized to the expected FIR luminosities  $L_{\text{IR}}^{(\text{exp})}$  presented in Table 4. As can be seen in Figure 15, the tight upper limits on the flux densities from the optical to the near-infrared wavelengths rule out the possibilities that the detected line is the CO lines. If we adopt the CO excitation ladder of Milky Way (Figure 4 of Carilli & Walter 2013) instead of the M82 ladder, we obtain higher FIR luminosities and thus larger normalization factors of the expected galaxy SEDs than those with the M82 CO ladder, which are ruled out by the upper limits from the optical to near-infrared. The possibility of [C $\text{I}$ ](1–0) is also excluded by the upper limits at the optical and the near-infrared wavelengths. In the case of [C $\text{II}$ ]158 $\mu\text{m}$ , the SEDs of the blue galaxies (M51 and NGC 6946) are ruled out, while

TABLE 5  
UPPER LIMITS ON THE FLUX DENSITIES OF SME-1

Instrument	Band/Wavelength	Magnitude/Flux Density ( $3\sigma$ limit, total)	Remark
Suprime-Cam	<i>B</i>	28.3 mag	(a)
Suprime-Cam	<i>V</i>	28.0 mag	(a)
Suprime-Cam	<i>R</i>	27.8 mag	(a)
Suprime-Cam	<i>i'</i>	27.7 mag	(a)
Suprime-Cam	<i>z'</i>	27.2 mag	(a)
WFC3	F098M	28.4 mag	(a)
WFC3	F125W	28.5 mag	(a)
WFCAM	<i>J</i>	26.0 mag	(a)
WFC3	F160W	28.1 mag	(a)
WFCAM	<i>H</i>	25.5 mag	(a)
WFCAM	<i>K</i>	25.8 mag	(a)
IRAC	3.6 $\mu\text{m}$	25.2 mag	(b)
IRAC	4.5 $\mu\text{m}$	25.2 mag	(b)
IRAC	5.8 $\mu\text{m}$	22.0 mag	(c)
IRAC	8.0 $\mu\text{m}$	21.8 mag	(c)
MIPS	24 $\mu\text{m}$	19.8 mag	(c)
SPIRE	250 $\mu\text{m}$	6.7 mJy	(d)
SPIRE	350 $\mu\text{m}$	5.6 mJy	(d)
SPIRE	500 $\mu\text{m}$	8.0 mJy	(d)
ALMA	1.2 mm	64 $\mu\text{Jy}$	(e)

NOTES. — (a) Measured within a  $2\times$  FWHM diameter aperture and corrected to total magnitude in a similar manner to McLure et al. (2013), assuming a point source and that the aperture depth is  $0.3 - 0.4$  mag deeper. (b) Calculated over a  $2''.4$  diameter aperture and corrected to total magnitude using the offset values listed in Table 2 of Ashby et al. (2013). (c) Measurements obtained in Ouchi et al. (2009). (d) Taken from Table 5 of Oliver et al. (2012). (e) Corrected for primary beam attenuation.

the SEDs of the galaxies with red colors (Arp220 and M82) are consistent with the upper limits on the flux densities at wavelengths from the optical to 1.2 mm.

In summary, the possibilities of the CO lines and the [CII](1–0) line have been excluded, but that of the [CII] line with the red SEDs (Arp220 and M82) is not ruled out. Finally, we examine another possibility: the possibility that the detected line is [OIII]88 $\mu\text{m}$  from a galaxy at  $z = 12.6$ . Since [OIII]88 $\mu\text{m}$  is one of the strongest FIR lines from HII regions, Inoue et al. (2014) have derived a line emissivity model for the [OIII]88 $\mu\text{m}$  line as a function of metallicity with the photoionization code CLOUDY (Ferland et al. 2013). We adopt the line emissivity model to estimate the total SFRs from the [OIII]88 $\mu\text{m}$  line luminosity, and test whether the estimated SFRs are consistent with the upper limits on the flux densities of SME-1 obtained from the *K*-band and ALMA Band 6 observations, which correspond to the rest-frame UV ( $\sim 1600\text{\AA}$ ) and FIR, respectively. We do not use the upper limit estimated from the WFC3 F160W image, since in this case, the redshifted Ly $\alpha$  and the continuum break enters the F160W band. The upper limit of the *K*-band data gives the upper limit of the unobscured SFR,  $\text{SFR}_{\text{UV}} \simeq 20 M_{\odot} \text{ yr}^{-1}$  (Kennicutt 1998a). Based on the ALMA Band 6 continuum data, the upper limit of the obscured SFR is estimated to be  $\text{SFR}_{\text{IR}} \simeq 40 M_{\odot} \text{ yr}^{-1}$  by the same method as noted in Section 1. Thus, if the total SFR expected from the line flux is higher than their sum,  $\text{SFR}_{\text{UV}} + \text{SFR}_{\text{IR}} \gtrsim 60 M_{\odot} \text{ yr}^{-1}$ , the possibility of [OIII]88 $\mu\text{m}$  is excluded. Based on Figure 1 of Inoue et al. (2014), if the galaxy metallicity is lower than  $0.16 Z_{\odot}$  or higher than  $0.32 Z_{\odot}$ , the total SFRs estimated from the [OIII]88 $\mu\text{m}$  luminosity are higher than  $60 M_{\odot} \text{ yr}^{-1}$ . Thus, the possibility of [OIII]88 $\mu\text{m}$  is ruled out if the galaxy metallicity is  $Z/Z_{\odot} \lesssim 0.2$  or  $Z/Z_{\odot} \gtrsim 0.3$ ; [OIII]88 $\mu\text{m}$  is pos-

sible only in the cases of  $Z/Z_{\odot} \simeq 0.2 - 0.3$ . The estimated total SFR based on Figure 1 of Inoue et al. (2014) has a minimum of about  $50 M_{\odot} \text{ yr}^{-1}$  at  $Z = 0.2 Z_{\odot}$ . Note that many observational studies have reported that the number density of star-forming galaxies at high redshifts ( $z \gtrsim 7$ ) decreases with increasing redshift (e.g., Bouwens et al. 2011; Ellis et al. 2013; Schenker et al. 2013; McLure et al. 2013; Coe et al. 2013; Oesch et al. 2013). Although this implies that it is unlikely that a rare high-redshift galaxy with an intense star formation of  $50 - 60 M_{\odot} \text{ yr}^{-1}$  is identified in our small field of view, the possibility of [OIII]88 $\mu\text{m}$  cannot be excluded from the current observational data.

To summarize the above, we have reported the detections of the SME candidates and discussed the possible interpretations for the line of SME-1. We have found that the possible interpretations are [CII]158 $\mu\text{m}$  from a dusty star-forming galaxy at  $z = 6.60$  or [OIII]88 $\mu\text{m}$  from a moderately metal-enriched star-forming galaxy at  $z = 12.6$ . If the detected line is [CII]158 $\mu\text{m}$ , SME-1 would be at a similar redshift to Himiko. In this case, the galaxy would be at a projected distance of  $\simeq 34$  proper kpc ( $\simeq 260$  kpc in comoving units) from Himiko. These systems might merge into a single galaxy.

Although the SME candidates show significant line detections, again we do not rule out the possibility that they are caused by unknown systematic noise effects as discussed above. Our carried-over ALMA cycle 1 program for Himiko will observe the SME candidates. The carried-over observations will give us an opportunity to carefully test whether the SME candidates are real or not.

## 7. SUMMARY

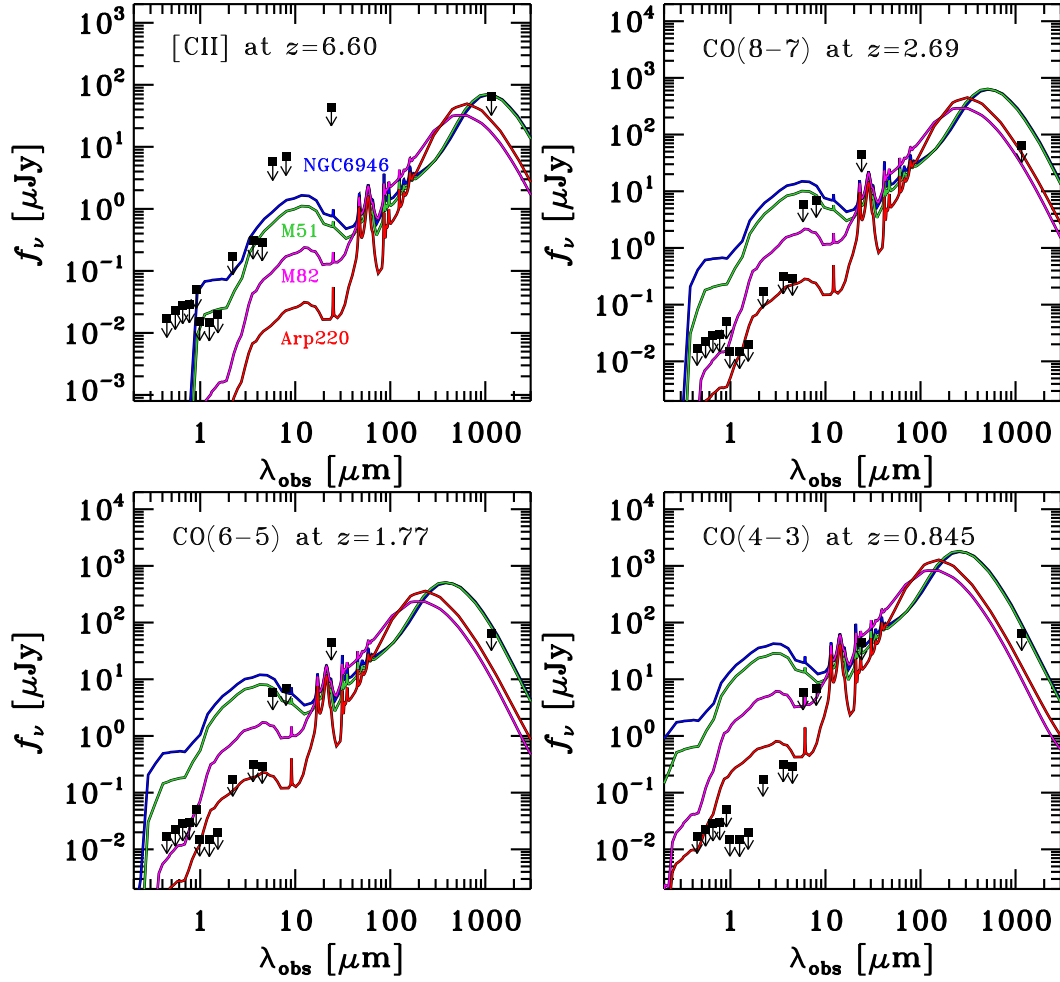


FIG. 15.— Multiwavelength SED of SME-1. The vertical arrows with filled squares show upper limits for Subaru/Suprime-Cam  $B$ ,  $V$ ,  $R$ ,  $i'$ ,  $z'$ ,  $HST$ /WFC3 F098M, F125W, F160W, UKIRT/WFCAM  $K$ , *Spitzer*/IRAC  $3.6\mu\text{m}$ ,  $4.5\mu\text{m}$ ,  $5.8\mu\text{m}$ ,  $8.0\mu\text{m}$ , *Spitzer*/MIPS  $24\mu\text{m}$ , and ALMA Band 6 from left to right. For comparison, we plot the redshifted SEDs of Arp220 (red line), M82 (magenta line), M51 (green line), and NGC 6946 (blue line) from Silva et al. (1998), scaled to the expected FIR luminosities from the detected line flux for four cases: [CII] $158\mu\text{m}$  (upper-left), CO(8-7) (upper-right), CO(6-5) (bottom-left), and CO(4-3) (bottom-right). The upper limits estimated from the *Herschel* SPIRE data are not shown, since they are shallow and affected by source confusion as shown in Figure 13.

In this paper, we have presented the number counts and the spatial clustering of faint SMGs, and reported serendipitous detections of SMEs with no multiwavelength continuum counterpart revealed by the deep ALMA observations. Exploiting the deep ALMA Band 6/Band 7 continuum data for the 10 independent fields that reduce the effect of cosmic variance, we have detected faint SMGs with flux densities of  $0.1 - 1.0$  mJy. In addition, we have conducted a blind search for line emitters in the ALMA data cubes, and identified five SME candidates. Our main results are as follows.

- We have constructed the  $1.2$  mm differential number counts of SMGs and found that the number counts increase with decreasing flux density down to  $0.1$  mJy. We have also found that the slope of the number counts for the faint ( $0.1 - 1$  mJy, or  $\text{SFR}_{\text{IR}} \sim 30 - 300 M_{\odot} \text{ yr}^{-1}$ ) SMGs is smaller than that for bright ( $> 1$  mJy) SMGs. Our number counts have revealed that the faint SMGs contribute about 50% of the EBL, which is significantly larger than the contributions from the bright SMGs ( $\sim 7\%$ ). The remaining 40% of the EBL is

contributed by very faint SMGs with flux densities of  $< 0.1$  mJy ( $\text{SFR}_{\text{IR}} \lesssim 30 M_{\odot} \text{ yr}^{-1}$ ).

- From the field-to-field scatter in their number counts, we have estimated the galaxy bias of the faint SMGs to be  $b_g \sim 2$ , which suggests that the dark halo masses of the faint SMGs is  $M_{\text{DH}} \sim 10^{12} M_{\odot}$ . Their bias is found to be lower than those of bright SMGs (Webb et al. 2003; Blain et al. 2004; Weiß et al. 2009; Hickox et al. 2012), indicating the clustering segregation with the FIR luminosity in SMGs. We also find that abundant star-forming galaxy populations at high redshifts such as sBzKs, LBGs, and LAEs have comparable galaxy bias values to that of the faint SMGs, which implies that some of the faint SMGs might be their FIR counterparts.
- We have found that the SME candidates have no counterpart in the multiwavelength images, suggesting that they would be faint galaxies at high redshifts. One of the SME candidates, SME-1, shows a significant line detection with an SNR of

7.1 at 249.9 GHz. Taking advantage of the upper limits estimated from the deep images at wavelengths from the optical to 1.2 mm, we have discussed what the detected line and the redshift of SME-1 are. If the detection of SME-1 is not induced by unknown systematic noise effects in ALMA data, the possible explanations for the detected line of SME-1 are [CII]158 $\mu$ m from a dusty star-forming galaxy at  $z = 6.60$  or [OIII]88 $\mu$ m from a star-forming galaxy with a moderate metallicity of  $Z/Z_{\odot} \simeq 0.2 - 0.3$  at  $z = 12.6$ .

#### ACKNOWLEDGEMENTS

We thank Bunyo Hatsukade for giving us helpful advice on analyzing the data and sending their results. We also thank Christopher C. Hayward and Ikko Shimizu for giving us their model predictions of the differen-

tial number counts. We appreciate the support of the staff at the ALMA Regional Center, especially Kazuya Saigo, Daisuke Iono, and Shinya Komugi. This work was supported by Japan Society for the Promotion of Science (JSPS), KAKENHI, Grants-in-Aid for Research Activity Start-up Grant Number 24840010 and Grant-in-Aid for Scientific Research (A) Grant Number 23244025. This work was also supported by World Premier International Research Center Initiative (WPI Initiative), MEXT, Japan. This paper makes use of the following ALMA data: ADS/JAO.ALMA#2011.0.00115.S, #2012.1.00602.S, #2011.0.00206.S, #2011.0.00243.S, and #2011.0.00268.S. ALMA is a partnership of ESO (representing its member states), NSF (USA) and NINS (Japan), together with NRC (Canada) and NSC and ASIAA (Taiwan), in cooperation with the Republic of Chile. The Joint ALMA Observatory is operated by ESO, AUI/NRAO and NAOJ.

#### REFERENCES

- Adelberger, K. L., Steidel, C. C., Giavalisco, M., et al. 1998, *ApJ*, 505, 18
- Adelberger, K. L., Steidel, C. C., Pettini, M., et al. 2005, *ApJ*, 619, 697
- Aretxaga, I., Wilson, G. W., Aguilar, E., et al. 2011, *MNRAS*, 415, 3831
- Ashby, M. L. N., Willner, S. P., Fazio, G. G., et al. 2013, *ApJ*, 769, 80
- Austermann, J. E., Aretxaga, I., Hughes, D. H., et al. 2009, *MNRAS*, 393, 1573
- Austermann, J. E., Dunlop, J. S., Perera, T. A., et al. 2010, *MNRAS*, 401, 160
- Bahcall, N. A., Dong, F., Hao, L., et al. 2003, *ApJ*, 599, 814
- Barger, A. J., Cowie, L. L., & Sanders, D. B. 1999, *ApJ*, 518, L5
- Barger, A. J., Cowie, L. L., Sanders, D. B., et al. 1998, *Nature*, 394, 248
- Barger, A. J., Wang, W.-H., Cowie, L. L., et al. 2012, *ApJ*, 761, 89
- Baugh, C. M., Lacey, C. G., Frenk, C. S., et al. 2005, *MNRAS*, 356, 1191
- Bertin, E., & Arnouts, S. 1996, *A&AS*, 117, 393
- Blain, A. W., Chapman, S. C., Smail, I., & Ivison, R. 2004, *ApJ*, 611, 725
- Blain, A. W., Smail, I., Ivison, R. J., Kneib, J.-P., & Frayer, D. T. 2002, *Phys. Rep.*, 369, 111
- Blanc, G. A., Lira, P., Barrientos, L. F., et al. 2008, *ApJ*, 681, 1099
- Borys, C., Chapman, S., Halpern, M., & Scott, D. 2003, *MNRAS*, 344, 385
- Bouwens, R. J., Illingworth, G. D., Oesch, P. A., et al. 2011, *ApJ*, 737, 90
- Bower, R. G., Benson, A. J., Malbon, R., et al. 2006, *MNRAS*, 370, 645
- Carilli, C. L., & Walter, F. 2013, *ARA&A*, 51, 105
- Casey, C. M., Narayanan, D., & Cooray, A. 2014, *ArXiv e-prints* (arXiv:1402.1456)
- Chapman, S. C., Blain, A. W., Smail, I., & Ivison, R. J. 2005, *ApJ*, 622, 772
- Chen, C.-C., Cowie, L. L., Barger, A. J., et al. 2013, *ApJ*, 762, 81
- Chen, C.-C., Cowie, L. L., Wang, W.-H., Barger, A. J., & Williams, J. P. 2011, *ApJ*, 733, 64
- Coe, D., Zitrin, A., Carrasco, M., et al. 2013, *ApJ*, 762, 32
- Combes, F., Rex, M., Rawle, T. D., et al. 2012, *A&A*, 538, L4
- Condon, J. J. 1974, *ApJ*, 188, 279
- Coppin, K., Chapin, E. L., Mortier, A. M. J., et al. 2006, *MNRAS*, 372, 1621
- Coppin, K., Halpern, M., Scott, D., et al. 2008, *MNRAS*, 384, 1597
- Coppin, K. E. K., Swinbank, A. M., Neri, R., et al. 2007, *ApJ*, 665, 936
- Cowie, L. L., Barger, A. J., & Kneib, J.-P. 2002, *AJ*, 123, 2197
- Croton, D. J., Springel, V., White, S. D. M., et al. 2006, *MNRAS*, 365, 11
- Daddi, E., Bournaud, F., Walter, F., et al. 2010, *ApJ*, 713, 686
- Davies, L. J. M., Bremer, M. N., Stanway, E. R., & Lehnert, M. D. 2013, *MNRAS*, 433, 2588
- Decarli, R., Smail, I., Walter, F., et al. 2014, *ApJ*, 780, 115
- Dole, H., Lagache, G., Puget, J.-L., et al. 2006, *A&A*, 451, 417
- Eales, S., Lilly, S., Gear, W., et al. 1999, *ApJ*, 515, 518
- Eales, S., Lilly, S., Webb, T., et al. 2000, *AJ*, 120, 2244
- Ellis, R. S., McLure, R. J., Dunlop, J. S., et al. 2013, *ApJ*, 763, L7
- Farrah, D., Lebouteiller, V., Spoon, H. W. W., et al. 2013, *ApJ*, 776, 38
- Ferland, G. J., Porter, R. L., van Hoof, P. A. M., et al. 2013, *Rev. Mexicana Astron. Astrofis.*, 49, 137
- Fixsen, D. J., Dwek, E., Mather, J. C., Bennett, C. L., & Shafer, R. A. 1998, *ApJ*, 508, 123
- Fontanot, F., Monaco, P., Silva, L., & Grazian, A. 2007, *MNRAS*, 382, 903
- Fry, J. N. 1996, *ApJ*, 461, L65
- Furusawa, H., Kosugi, G., Akiyama, M., et al. 2008, *ApJS*, 176, 1
- Furusawa, J., Sekiguchi, K., Takata, T., et al. 2011, *ApJ*, 727, 111
- Gawiser, E., Francke, H., Lai, K., et al. 2007, *ApJ*, 671, 278
- Gehrels, N. 1986, *ApJ*, 303, 336
- Giavalisco, M., & Dickinson, M. 2001, *ApJ*, 550, 177
- Girardi, M., Boschin, W., & da Costa, L. N. 2000, *A&A*, 353, 57
- Granato, G. L., De Zotti, G., Silva, L., Bressan, A., & Danese, L. 2004, *ApJ*, 600, 580
- Grazian, A., Fontana, A., Moscardini, L., et al. 2006, *A&A*, 453, 507
- Greve, T. R., Ivison, R. J., Bertoldi, F., et al. 2004, *MNRAS*, 354, 779
- Greve, T. R., Bertoldi, F., Smail, I., et al. 2005, *MNRAS*, 359, 1165
- Grogin, N. A., Kocevski, D. D., Faber, S. M., et al. 2011, *ApJS*, 197, 35
- Guaita, L., Gawiser, E., Padilla, N., et al. 2010, *ApJ*, 714, 255
- Hasegawa, K., & Semelin, B. 2013, *MNRAS*, 428, 154
- Hatsukade, B., Ohta, K., Seko, A., Yabe, K., & Akiyama, M. 2013, *ApJ*, 769, L27
- Hatsukade, B., Kohno, K., Aretxaga, I., et al. 2011, *MNRAS*, 411, 102
- Hauser, M. G., & Dwek, E. 2001, *ARA&A*, 39, 249
- Hauser, M. G., Arendt, R. G., Kelsall, T., et al. 1998, *ApJ*, 508, 25
- Hayashi, M., Shimasaku, K., Motohara, K., et al. 2007, *ApJ*, 660, 72
- Hayward, C. C., Narayanan, D., Kereš, D., et al. 2013, *MNRAS*, 428, 2529
- Hickox, R. C., Wardlow, J. L., Smail, I., et al. 2012, *MNRAS*, 421, 284
- Hodge, J. A., Karim, A., Smail, I., et al. 2013, *ApJ*, 768, 91
- Hogg, D. W., & Turner, E. L. 1998, *PASP*, 110, 727



- Holland, W. S., Robson, E. I., Gear, W. K., et al. 1999, *MNRAS*, 303, 659
- Hughes, D. H., Serjeant, S., Dunlop, J., et al. 1998, *Nature*, 394, 241
- Ichikawa, T., Suzuki, R., Tokoku, C., et al. 2007, *PASJ*, 59, 1081
- Inoue, A. K., Shimizu, I., Tamura, Y., et al. 2014, *ApJ*, 780, L18
- Iono, D., Wilson, C. D., Yun, M. S., et al. 2009, *ApJ*, 695, 1537
- Ivison, R. J., Greve, T. R., Dunlop, J. S., et al. 2007, *MNRAS*, 380, 199
- Johansson, D., Sigurdarson, H., & Horellou, C. 2011, *A&A*, 527, A117
- Kanekar, N., Wagg, J., Ram Chary, R., & Carilli, C. L. 2013, *ApJ*, 771, L20
- Karim, A., Swinbank, A. M., Hodge, J. A., et al. 2013, *MNRAS*, 432, 2
- Kennicutt, Jr., R. C. 1998a, *ARA&A*, 36, 189
- . 1998b, *ApJ*, 498, 541
- Knudsen, K. K., van der Werf, P. P., & Kneib, J. 2008, *MNRAS*, 384, 1611
- Koekemoer, A. M., Faber, S. M., Ferguson, H. C., et al. 2011, *ApJS*, 197, 36
- Kovács, A., Chapman, S. C., Dowell, C. D., et al. 2006, *ApJ*, 650, 592
- Lacey, C., & Cole, S. 1993, *MNRAS*, 262, 627
- Lagache, G., Puget, J.-L., & Dole, H. 2005, *ARA&A*, 43, 727
- Lawrence, A., Warren, S. J., Almaini, O., et al. 2007, *MNRAS*, 379, 1599
- Lee, K.-S., Alberts, S., Atlee, D., et al. 2012, *ApJ*, 758, L31
- Lee, K.-S., Giavalisco, M., Gnedin, O. Y., et al. 2006, *ApJ*, 642, 63
- Lin, L., Dickinson, M., Jian, H.-Y., et al. 2012, *ApJ*, 756, 71
- Lupu, R. E., Scott, K. S., Aguirre, J. E., et al. 2012, *ApJ*, 757, 135
- Mao, R. Q., Henkel, C., Schulz, A., et al. 2000, *A&A*, 358, 433
- McLure, R. J., Dunlop, J. S., Bowler, R. A. A., et al. 2013, *MNRAS*, 432, 2696
- McMullin, J. P., Waters, B., Schiebel, D., Young, W., & Golap, K. 2007, in *Astronomical Society of the Pacific Conference Series*, Vol. 376, *Astronomical Data Analysis Software and Systems XVI*, ed. R. A. Shaw, F. Hill, & D. J. Bell, 127
- Mo, H. J., & White, S. D. M. 2002, *MNRAS*, 336, 112
- Nagao, T., Maiolino, R., De Breuck, C., et al. 2012, *A&A*, 542, L34
- Nakajima, K., Ouchi, M., Shimasaku, K., et al. 2012, *ApJ*, 745, 12
- Norberg, P., Cole, S., Baugh, C. M., et al. 2002, *MNRAS*, 336, 907
- Oesch, P. A., Bouwens, R. J., Illingworth, G. D., et al. 2013, *ApJ*, 773, 75
- Okamoto, T., Frenk, C. S., Jenkins, A., & Theuns, T. 2010, *MNRAS*, 406, 208
- Oke, J. B., & Gunn, J. E. 1983, *ApJ*, 266, 713
- Oliver, S. J., Bock, J., Altieri, B., et al. 2012, *MNRAS*, 424, 1614
- Omont, A., Neri, R., Cox, P., et al. 2011, *A&A*, 530, L3
- Omont, A., Yang, C., Cox, P., et al. 2013, *A&A*, 551, A115
- Ouchi, M., Yamada, T., Kawai, H., & Ohta, K. 1999, *ApJ*, 517, L19
- Ouchi, M., Shimasaku, K., Okamura, S., et al. 2004, *ApJ*, 611, 685
- Ouchi, M., Ono, Y., Egami, E., et al. 2009, *ApJ*, 696, 1164
- Ouchi, M., Shimasaku, K., Furusawa, H., et al. 2010, *ApJ*, 723, 869
- Ouchi, M., Ellis, R., Ono, Y., et al. 2013, *ApJ*, 778, 102
- Overzier, R. A., Bouwens, R. J., Illingworth, G. D., & Franx, M. 2006, *ApJ*, 648, L5
- Peebles, P. J. E. 1993, *Principles of Physical Cosmology*, ed. Peebles, P. J. E.
- Perera, T. A., Chapin, E. L., Austermann, J. E., et al. 2008, *MNRAS*, 391, 1227
- Puget, J.-L., Abergel, A., Bernard, J.-P., et al. 1996, *A&A*, 308, L5
- Quadri, R., van Dokkum, P., Gawiser, E., et al. 2007, *ApJ*, 654, 138
- Reddy, N., Dickinson, M., Elbaz, D., et al. 2012, *ApJ*, 744, 154
- Riechers, D. A., Bradford, C. M., Clements, D. L., et al. 2013, *Nature*, 496, 329
- Robertson, B. E. 2010, *ApJ*, 716, L229
- Schechter, P. 1976, *ApJ*, 203, 297
- Schenker, M. A., Robertson, B. E., Ellis, R. S., et al. 2013, *ApJ*, 768, 196
- Scott, K. S., Yun, M. S., Wilson, G. W., et al. 2010, *MNRAS*, 405, 2260
- Scott, K. S., Wilson, G. W., Aretxaga, I., et al. 2012, *MNRAS*, 423, 575
- Scott, S. E., Dunlop, J. S., & Serjeant, S. 2006, *MNRAS*, 370, 1057
- Scott, S. E., Fox, M. J., Dunlop, J. S., et al. 2002, *MNRAS*, 331, 817
- Sheth, R. K., & Tormen, G. 1999, *MNRAS*, 308, 119
- Shimizu, I., Yoshida, N., & Okamoto, T. 2012, *MNRAS*, 427, 2866
- Silva, L., Granato, G. L., Bressan, A., & Danese, L. 1998, *ApJ*, 509, 103
- Siringo, G., Kreysa, E., Kovács, A., et al. 2009, *A&A*, 497, 945
- Smail, I., Ivison, R. J., & Blain, A. W. 1997, *ApJ*, 490, L5
- Smail, I., Ivison, R. J., Blain, A. W., & Kneib, J.-P. 2002, *MNRAS*, 331, 495
- Smolčić, V., Aravena, M., Navarrete, F., et al. 2012, *A&A*, 548, A4
- Solomon, P. M., Downes, D., & Radford, S. J. E. 1992, *ApJ*, 398, L29
- Solomon, P. M., & Vanden Bout, P. A. 2005, *ARA&A*, 43, 677
- Springel, V., & Hernquist, L. 2003, *MNRAS*, 339, 289
- Stacey, G. J., Hailey-Dunsheath, S., Ferkinhoff, C., et al. 2010, *ApJ*, 724, 957
- Swinbank, A. M., Karim, A., Smail, I., et al. 2012, *MNRAS*, 427, 1066
- Tacconi, L. J., Neri, R., Chapman, S. C., et al. 2006, *ApJ*, 640, 228
- Tacconi, L. J., Genzel, R., Smail, I., et al. 2008, *ApJ*, 680, 246
- Tadaki, K.-i., Kodama, T., Tamura, Y., et al. 2014, *ArXiv e-prints* (arXiv:1403.0040)
- Tamura, Y., Saito, T., Tsuru, T. G., et al. 2014, *ApJ*, 781, L39
- Ueda, Y., Watson, M. G., Stewart, I. M., et al. 2008, *ApJS*, 179, 124
- van der Werf, P. P., Berciano Alba, A., Spaans, M., et al. 2011, *ApJ*, 741, L38
- Walter, F., Weiß, A., Downes, D., Decarli, R., & Henkel, C. 2011, *ApJ*, 730, 18
- Wang, R., Wagg, J., Carilli, C. L., et al. 2013, *ApJ*, 773, 44
- Wang, W.-H., Cowie, L. L., & Barger, A. J. 2004, *ApJ*, 613, 655
- Wang, W.-H., Cowie, L. L., Barger, A. J., & Williams, J. P. 2011, *ApJ*, 726, L18
- Ward, J. S., Zmuidzinas, J., Harris, A. I., & Isaak, K. G. 2003, *ApJ*, 587, 171
- Warren, S. J., Hambly, N. C., Dye, S., et al. 2007, *MNRAS*, 375, 213
- Webb, T. M., Eales, S., Foucaud, S., et al. 2003, *ApJ*, 582, 6
- Weiß, A., Downes, D., Walter, F., & Henkel, C. 2005a, *A&A*, 440, L45
- Weiß, A., Walter, F., & Scoville, N. Z. 2005b, *A&A*, 438, 533
- Weiß, A., Kovács, A., Coppin, K., et al. 2009, *ApJ*, 707, 1201
- Willott, C. J., Omont, A., & Bergeron, J. 2013, *ApJ*, 770, 13
- Wilson, G. W., Austermann, J. E., Perera, T. A., et al. 2008, *MNRAS*, 386, 807
- Yang, C., Gao, Y., Omont, A., et al. 2013, *ApJ*, 771, L24
- Yoshida, M., Shimasaku, K., Ouchi, M., et al. 2008, *ApJ*, 679, 269
- Yun, M. S., Scott, K. S., Guo, Y., et al. 2012, *MNRAS*, 420, 957
- Zehavi, I., Zheng, Z., Weinberg, D. H., et al. 2005, *ApJ*, 630, 1
- . 2011, *ApJ*, 736, 59